Int. J. Appl. Math. Comput. Sci., 2026, Vol. 36, No. 3, 505–525
DOI: 10.61822/amcs-2026-0033

PARAMETER IDENTIFICATION OF BEARING STIFFNESS FOR A CENTRIFUGAL COMPRESSOR USING AN ARTIFICIAL NEURAL NETWORK

IVAN PAVLENKO [a], OLEKSANDR ROSHCHUPKIN [a], MAREK OCHOWIAK [b], ANDŻELIKA KRUPIŃSKA [b], MICHAŁ DOLIGALSKI [c,*], JACEK TKACZ [c]

[a] Volodymyr Martsynkovskyy Department of Computational Mechanics
Sumy State University
Kharkivska 116, 40007, Sumy, Ukraine
e-mail: {i.pawlenko,o.roshchupkin}@cm.sumdu.edu.ua

[b] Institute of Chemical Technology and Engineering
Poznań University of Technology
Berdychowo 4, 60-695 Poznań, Poland
e-mail: {marek.ochwiak,andzelika.krupinska}@put.poznan.pl

[c] Institute of Metrology, Electronics and Computer Science
University of Zielona Góra
Licealna 9, 65-417 Zielona Góra, Poland
e-mail: {m.doligalski,j.tkacz}@imei.uz.zgora.pl

The design of modern high-tech equipment (pumps, compressors, turbines) is inevitably related to the need to ensure vibration reliability, especially at high shaft rotation speeds, which is particularly relevant for flexible rotors. Therefore, the research aims to provide vibration reliability of energy-intensive rotary machines by developing a hybrid parametric identification approach that leverages analytical dependencies in rotor dynamics, numerical simulations to study rotor behavior, and artificial intelligence systems. While implementing the proposed solution, the Monte Carlo method and Moore–Penrose pseudoinversion are also applied. As a result, modified linear and nonlinear parameter identification approaches are developed. They are based on an improved finite element model that accounts for the analytical dependence of bearing stiffness on rotor speed, with the parameters evaluated numerically. The corresponding algorithms were implemented in the PTC MathCAD 14 computer algebra system and the Python 3.13 programming language, using the authors' program code and an artificial neural network. The developed methods and algorithms were proven in the case study of a natural gas compressor station's multistage centrifugal compressor, S325 GC2-650/6-56M12. As a result, stiffness parameters of bearing supports were identified with a 0.2–0.7% accuracy for the first two critical frequencies compared with the available data from the accelerating-balancing stand "Schenck" with a vacuum chamber. The proposed parameter identification approach can also be extended to evaluate stiffness parameters for high-precision bearing supports with speed-dependent stiffness in multistage centrifugal pumps, turbochargers, turbines, and turbopump units.

Keywords: rotor dynamics, process innovation, finite element analysis, critical frequency, Monte Carlo method, regression analysis, Moore–Penrose pseudoinverse, artificial intelligence, energy efficiency.

1. Introduction

The operation of modern energy equipment is directly controlled by high-speed rotary machines (Elsamanty *et al.*, 2023), e.g., pumps, compressors, turbines, and turbopump units. A permanent increase in their operating parameters (pressure, flow rate) and a decrease in their mass-dimensional characteristics are associated with an increase in the rotation speed of a rotor, which is the central, highly loaded part of power machines (Dong

*Corresponding author

et al., 2022).

The above trends inevitably lead to problems in increasing the reliability of rotary systems. Successfully solving these issues increases the efficiency and durability of the relevant industrial installations (Gawde *et al*., 2023). This is conducted at each stage of the production and exploitation of rotary machines:

- *at the design stage*: through rational choice of bearing supports and gap seals and ensuring their dynamic characteristics (e.g., stiffness and damping coefficients) (Hui *et al*., 2024), compliance with strict tolerances for the manufacture of flow parts, including impeller blades (Chelabi *et al*., 2022);
- *in manufacturing*: by using precision materials for shafts and bushing parts with high strength and fatigue resistance (Tarelnyk and Martsynkovskyy, 2014), application of high-precision machining technologies (Stelmakh *et al*., 2023), control of the total radial clearance (Manikandan and Rajasekhara, 2025), use of non-destructive testing methods (Bachschmid *et al*., 2010);
- *during assembly*: by employing special stands and automated assembly accuracy control systems (Ivanov *et al*., 2022);
- *before the operation*: by performing dynamic balancing on a special accelerating-balancing stand with a vacuum chamber to reduce the residual imbalance according to the requirements of the international standards: ISO 1940-1:2023 for rigid shafts, which operate at speeds significantly lower than the first critical frequency (Nogill, 2019), ISO 21940-12:2016 for flexible rotors (Hato, 2023) of centrifugal compressor, turbopump units, etc.;
- *during operation*: by installing external dampers to reduce the amplitude of vibrations and optimizing lubrication systems to reduce vibration loads (Ma *et al*., 2021).

One of the key problems at all the above stages is assessing bearing stiffness characteristics since the resonance detuning margin depends on them, especially for flexible rotors (Lee and Choi, 1997). In the corresponding machines, sliding bearings are installed, whose stiffness depends on shaft rotation speed, which significantly complicates the prediction of the dynamic behavior of the comprehensive hydromechanical system "rotor–bearing supports–gap seals" at the design stage (Yu *et al*., 2022).

A comparative analysis of the state of the art is presented in Table 1.

However, this problem can be solved before the operation by evaluating the stiffness parameters. Thus, the research goal is to ensure vibration reliability of energy-intensive rotary machines by developing a hybrid parametric identification approach, which consists in comprehensive use of analytical dependencies for rotor dynamics, numerical simulations for studying whirl behavior (FEM modeling with the authors' codes in MathCAD and Python) and artificial intelligence systems.

The main problem with existing FEM and ANN-based models is their inability to calculate bearing stiffness from physical and geometric parameters directly. Unfortunately, such an approach does not allow improving bearing stiffness models. Despite this, an inverse approach should be proposed to estimate the bearing stiffness parameters from data, with frequencies as inputs and the unknown bearing stiffness coefficients as evaluation parameters.

Therefore, the proposed approach allows solving the problem of vibration reliability at the design stage by properly detuning resonances based on evaluations of bearing stiffness parameters. For this purpose, FEM models implemented in MathCAD and Python are improved by adding a dependency between bearing stiffness and shaft rotation speed. Moreover, an approach to evaluate the coefficients of these dependencies is proposed using the Moore–Penrose pseudoinverse and an artificial neural network (ANN).

2. Literature review

The scientific and practical significance of the proposed research is highlighted by the state-of-the-art in design, simulation, and modeling of rotor dynamics in terms of solving the problems of resonance detuning, the impact of design features and gap seals on rotor behavior, and an increase in the accuracy of finite element analysis, machine learning (ML), and artificial intelligence systems.

Laine *et al*. (2023) primarily addressed the resonance detuning problem by continuously adjusting the support stiffness. As a result, a foundation stiffness tuning strategy was implemented to ensure a resonance-free operating mode. However, implementing real-time adjustment is technically challenging due to limited applicability, high costs, enormous system complexity, and the need for advanced control systems, sensors, and actuators.

Also, Ran *et al*. (2024) proposed a method to attenuate lateral rotor vibrations using an axial control mechanism with resonance detuning. As a result, the effectiveness of the control mechanism for flexible rotors in an extended mode range was demonstrated. However, this approach requires precise coordination for effective operation. Potential delays in response time can limit it. Moreover, rotor lifespan can be reduced by applying additional axial loads to thrust bearings, thereby affecting long-term durability.

Table 1. Comparative literature review results.

Author(s) and references	Main focus	Methods and approaches	Key contribution	Main limitations	Gaps addressed in this work
Laine *et al.*, 2023	Resonance detuning	Real-time support stiffness tuning	Achieved resonance-free operation via adaptive stiffness	High system complexity, cost, and limited industrial applicability	Avoids real-time actuation; enables offline identification of speed-dependent stiffness
Ran *et al.*, 2024	Vibration attenuation via detuning	Axial control mechanism	Reduced lateral vibrations over an extended speed range	Response delays; added axial loads reduce thrust bearing life	No additional loads; stiffness identified without control of frequency
Makivskyi *et al.*, 2024	Rotor design features	Gap seals and design optimization	Reduced vibration amplitudes by up to 35% of radial clearance	Increased wear; unresolved sility; efficiency–frequency trade-off	Stability-focused modeling evaluating actual stiffness parameters of gap seals
Kondus *et al.*, 2020	Energy efficiency in pumps	Impeller blade configuration optimization	Increase by $+7\%$ in pressure head and efficiency	Primarily numerical; limited real-world effects considered	Focus on dynamic stability; limited stiffness identification
Brunetiére *et al.*, 2024	Rotor–seal interaction	Numerical simulation of gas seals	Revealed sensitivity to operating conditions	Limited transient validation; model sensitivity	Physics-consistent FEM with data-driven stiffness correction
Zahorulko *et al.*, 2023	Gap seal stability	Experimental evaluation	Identified hydrodynamic forces and dynamic coefficients	Complex experiments; limited generalizability	Avoids validation by actual frequencies via inverse FEM–ANN identification
Rao, 2011	Classical rotor dynamics	FEM, Campbell diagrams	Comprehensive summary of FEM approaches	Constant stiffness; steady-state assumptions	Allows arbitrary speed-independent stiffness
Kirchgäßner, 2016	Rotor dynamic modeling	FEM-based formulations	Systematization of modeling techniques	Limited to linear, constant-parameter systems	Partially extends FEM to nonlinear speed-dependent stiffness
Garpelli *et al.*, 2023	Rotor unbalance	ANN-based identification	Solved the unbalance estimation problem	Unbalance is largely linear per ISO standards	Partially addresses the nonlinear stiffness identification problem
Kalkat *et al.*, 2003	AI in rotor dynamics	ANN-based vibration analysis	Demonstrated ANN effectiveness	Cannot identify speed-dependent stiffness	Provides inverse identification of speed-independent bearing stiffness

Makivskyi *et al*. (2024) studied the impact of design features of the pump's rotor on vibration reliability. As a result, amplitudes of oscillations near the operating mode frequency were decreased by up to 35% of the radial gaps. Nevertheless, the proposed approach's main problems include potentially increased wear from gap seals and unresolved stability issues arising from a bearingless support design. Moreover, such an approach necessitates addressing the key trade-off between energy efficiency and increased frequency.

Also, Kondus *et al*. (2020) addressed design issues to improve energy efficiency of the operating process in torque-flow pumping units. As a result, the pressure head and energy efficiency were increased by 7% due to

a rational choice of the impeller blades' configuration. Nevertheless, the study is primarily based on numerical simulations that do not capture real-world conditions (e.g., turbulence, multiphase flow effects, and wear).

The fundamental issues in studying the impact of gap seals on rotor dynamics were addressed by Brunetière *et al*. (2024), who conducted numerical simulations of a compressor with impulse gas seals. However, the results exhibit some flow due to the sensitivity of the gas-dynamic system "rotor–gap seals–stator" to operating conditions (rotor speed, pressure, and chamber volume) and to limited validation at transient conditions. Zahorulko *et al*. (2023) experimentally studied static and dynamic rotor stability in gap seals to eliminate these disadvantages. As a result, hydrodynamic forces and the corresponding dynamic stiffness and damping coefficients were evaluated. However, sophisticated experimental research with precise measurement techniques is difficult to replicate in other laboratories. Also, the study has limited generalizability because it considers only the three-annular seals. Moreover, such a design with radial multi-gap seals poses manufacturing challenges and requires balancing stability, leakage, and intense wear.

A general approach to finite element analysis in rotor dynamics can be observed in the research of Rao (2011) and Kirchgäßner (2016), where initial approaches based on previous developments were summarized. However, critical speeds are evaluated using the Campbell diagram. Such an approach is though limited by steady-state conditions and constant elements of the stiffness matrix.

Garpelli *et al*. (2023) also considered ANNs as a numerical approach to solving the rotor unbalancing problem. As a result, a method for evaluating a system of imbalances was applied. Nevertheless, even for a flexible rotor, according to the international standard ISO 21940-12:2016, the residual imbalance values suggest that rotor balancing is a linear problem that can be solved using available approaches based on the inverse matrix of complex parameters (Pavlenko *et al*., 2019).

Kalkat *et al*. (2003) considered a general approach for studying rotor dynamics using artificial intelligence systems. As a result, the effectiveness of artificial neural networks in vibration analysis of rotor-bearing systems was shown. However, the proposed approach does not allow evaluating the initial system parameters, i.e., bearing stiffness, if they depend on rotor speed.

Given the above, the present research aims to improve the vibration reliability of rotary machines by more precisely evaluating bearing stiffness to achieve reliable resonance detuning. The following research objectives can be formulated to achieve this goal.

First, a finite element model of rotor dynamics should be formulated analytically, accounting for the effect of rotor speed on bearing stiffness. Second, an ML using the Moore–Penrose pseudoinverse should be applied to the developed finite-element rotor dynamics model to evaluate stiffness parameters in a first approximation. Third, an artificial neural network should be architected to clarify the evaluated stiffness parameters in a nonlinear problem formulation.

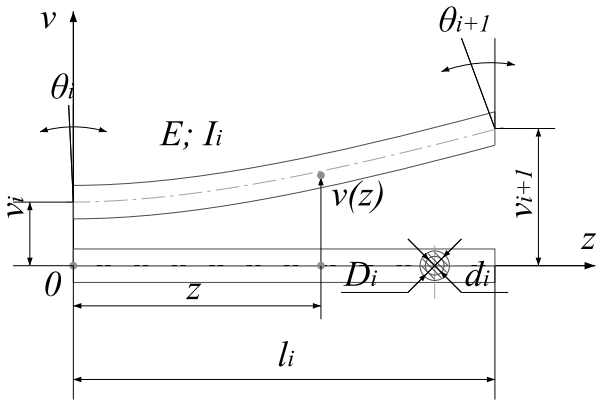


Fig. 1. Design scheme of the finite element.

The remainder of the article is organized as follows. Section 3 describes an improved finite element model of rotor dynamics for a centrifugal compressor, as well as a description of ways for ML evaluation of bearing stiffness using a modified Moore–Penrose pseudoinverse and nonlinear ANN-based parameter identification. It also presents the ANN-based stiffness correction approach.

Section 4 discusses numerical results and their consequent application as a dataset for ML-based evaluation of stiffness parameters and ANN training. It also includes ANN-based parameter evaluation results for actual critical frequencies.

Finally, Section 5 summarizes the main findings, scientific novelty, and practical significance, discusses the main advantages and shortcomings, and proposes further research directions.

3. Research methodology

3.1. Improved finite element model of rotor dynamics for a centrifugal compressor. Each mode shape can be considered a plane curve according to the fundamentals of eigenvalue problems in rotor dynamics. Therefore, a 2D finite element model entirely describes the rotor behavior near critical speeds. However, the assumption of isotropic bending stiffness of the shaft is recommended to be fulfilled.

A design scheme of the i-th finite element is presented in Fig. 1.

The following parameters are introduced: z, local longitudinal coordinate [m]; l_i, element's length [m]; E, Young's modulus of elasticity of the shaft material [N/m^2]; D_i, outer diameter [m]; d_i, inner diameter [m];

I_i, element's cross-sectional moment of inertia [m^4]; v_i, v_{i+1}, transversal nodal displacements [m]; θ_i, θ_{i+1}, deviation angles for the i-th and $(i+1)$-th cross-sections [rad].

For realizing a finite element analysis, a cubic polynomial form for transversal displacement $v(z)$ along the longitudinal coordinate z is set:

$$v(z) = \begin{Bmatrix} v_i \\ \theta_i \\ -\dfrac{3v_i}{l_i^2} - \dfrac{2\theta_i}{l_i} + \dfrac{3v_{i+1}}{l_i^2} - \dfrac{\theta_{i+1}}{l_i} \\ \dfrac{2v_i}{l_i^3} + \dfrac{\theta_i}{l_i^2} - \dfrac{2v_{i+1}}{l_i^3} + \dfrac{\theta_{i+1}}{l_i^2} \end{Bmatrix}^T \begin{Bmatrix} 1 \\ z \\ z^2 \\ z^3 \end{Bmatrix}. \tag{1}$$

The local stiffness and inertia matrices of the i-th finite element are as follows:

$$[K(\omega)]_i = \begin{bmatrix} k_{11}^{\langle i\rangle} & k_{12}^{\langle i\rangle} & k_{13}^{\langle i\rangle} & k_{14}^{\langle i\rangle} \\ k_{21}^{\langle i\rangle} & k_{22}^{\langle i\rangle} & k_{23}^{\langle i\rangle} & k_{24}^{\langle i\rangle} \\ k_{31}^{\langle i\rangle} & k_{32}^{\langle i\rangle} & k_{33}^{\langle i\rangle} & k_{34}^{\langle i\rangle} \\ k_{41}^{\langle i\rangle} & k_{42}^{\langle i\rangle} & k_{43}^{\langle i\rangle} & k_{44}^{\langle i\rangle} \end{bmatrix}, \tag{2}$$

$$[M]_i = \begin{bmatrix} m_{11}^{\langle i\rangle} & m_{12}^{\langle i\rangle} & m_{13}^{\langle i\rangle} & m_{14}^{\langle i\rangle} \\ m_{21}^{\langle i\rangle} & m_{22}^{\langle i\rangle} & m_{23}^{\langle i\rangle} & m_{24}^{\langle i\rangle} \\ m_{31}^{\langle i\rangle} & m_{32}^{\langle i\rangle} & m_{33}^{\langle i\rangle} & m_{34}^{\langle i\rangle} \\ m_{41}^{\langle i\rangle} & m_{42}^{\langle i\rangle} & m_{43}^{\langle i\rangle} & m_{44}^{\langle i\rangle} \end{bmatrix}, \tag{3}$$

where i is the element number, whose elements are determined as follows:

$$\begin{aligned} &k_{11}^{\langle i\rangle} = -k_{13}^{\langle i\rangle} = -k_{31}^{\langle i\rangle} = k_{33}^{\langle i\rangle} = \frac{12EI_i}{l_i^3}, \\ &k_{12}^{\langle i\rangle} = k_{14}^{\langle i\rangle} = k_{21}^{\langle i\rangle} = -k_{23}^{\langle i\rangle} \\ &\quad = -k_{32}^{\langle i\rangle} = -k_{34}^{\langle i\rangle} = k_{41}^{\langle i\rangle} = -k_{43}^{\langle i\rangle} = \frac{6EI_i}{l_i^2}, \\ &k_{22}^{\langle i\rangle} = 2k_{24}^{\langle i\rangle} = 2k_{42}^{\langle i\rangle} = k_{44}^{\langle i\rangle} = \frac{4EI_i}{l_i}, \end{aligned} \tag{4}$$

$$\begin{aligned} &m_{11}^{\langle i\rangle} = m_{33}^{\langle i\rangle} = \frac{13}{35}m_i; m_{13}^{\langle i\rangle} = m_{31}^{\langle i\rangle} = \frac{9}{70}m_i, \\ &m_{12}^{\langle i\rangle} = m_{21}^{\langle i\rangle} = -m_{34}^{\langle i\rangle} = -m_{43}^{\langle i\rangle} = \frac{11}{210}m_i l_i, \\ &-m_{14}^{\langle i\rangle} = m_{23}^{\langle i\rangle} = m_{32}^{\langle i\rangle} = -m_{41}^{\langle i\rangle} = \frac{13}{420}m_i l_i, \\ &m_{22}^{\langle i\rangle} = m_{44}^{\langle i\rangle} = \frac{1}{105}m_i l_i^2, m_{24}^{\langle i\rangle} = m_{42}^{\langle i\rangle} \\ &\quad = -\frac{11}{210}m_i l_i^2, \end{aligned} \tag{5}$$

where E is Young's modulus of elasticity for the shaft's material [N/m^2], I_i is an element's cross-sectional moments of inertia I_i [m^4], and m_i is an element's mass [kg]. The finite element's cross-sectional moment of inertia I_i and mass m_i are calculated as follows:

$$I_i = \frac{\pi}{64}\left(D_i^4 - d_i^4\right) l_i, \tag{6}$$

$$m_i = \frac{\pi}{4}p\left(D_i^2 - d_i^2\right) l_i. \tag{7}$$

The global stiffness and inertia matrices of the entire finite element model of rotor dynamics are obtained by summing the elements of matrices with similar node numbers.

As a result, the global stiffness and inertia matrices $[M_G]$ and $[K_G(\omega)]$ of the dimensions $(2n+2)\times(2n+2)$ are formed:

$$[M_G] = \sum_{i=1}^{n} G_4^{(2n+2)}\left([M]_i\right), \tag{8}$$

where n is the total number of finite elements and $G_4^{(2n+2)}\left([M]_i\right)$ is the matrix expansion operator from dimension 4×4 to dimension $(2n+2)\times(2n+2)$ by adding zero elements, except for the elements of the original matrix $[M]_i$, as the following 4×4 submatrix of the global one:

$$[M]_i = sub\left\{[M_G],\ (i,i),\ (i+3,\ i+3)\right\}. \tag{9}$$

The stiffness matrix $[K(\omega)]$ is globalized similarly to $[K_G(\omega)]$.

As a result, within the i-th finite element, the elements of the global matrices take the form of Eqns. ((10) and (11)).

The inertia matrix (11) includes Δm_i, i.e., the added mass of the i-th bushing part [kg].

Also, traditional finite element models assume constant bearing stiffness values evaluated at various rotor speeds ω [rad/s]. Such an approach necessitates graphically solving the eigenvalue problem using the Campbell diagram (Rao, 2011). An improved finite element model is used to eliminate this disadvantage, in which the stiffness matrix (10) includes the i-th bearing stiffness $c_i(\omega)$ as a function of the rotor speed ω.

The inner diameter is also included in the improved model to account for hollow shafts in turbines, turbochargers, turbopump units, and other applications.

They allow formulating the matrix equation of the rotor's free oscillations as follows:

$$[M_G]\frac{d^2}{dt^2}\{X\} + [K_G(\omega)]\{X\} = \{0\}, \tag{12}$$

where $[X]$ is the vector-column of size $(2n+2)\times 1$ containing nodal displacements, t is time [s] and $\{0\}$ is the zero-valued vector column $(2n+2)\times 1$.

For each p-th harmonic component

$$\{X\}_p = \{A\}_p \sin(\omega_p t), \tag{13}$$

accurate to the amplitude $\{A\}_p$ (the p-th mode shape, a column-vector of size $(2n+2)\times 1$), the eigenvalue

$$[K_G(\omega)]_i = \begin{bmatrix} k_{33}^{\langle i-1\rangle} + k_{11}^{\langle i\rangle} + c_i(\omega) & k_{34}^{\langle i-1\rangle} + k_{12}^{\langle i\rangle} & k_{13}^{\langle i\rangle} & k_{14}^{\langle i\rangle} \\ k_{43}^{\langle i\rangle} + k_{21}^{\langle i\rangle} & k_{44}^{\langle i\rangle} + k_{22}^{\langle i\rangle} & k_{23}^{\langle i\rangle} & k_{24}^{\langle i\rangle} \\ k_{31}^{\langle i\rangle} & k_{32}^{\langle i\rangle} & k_{33}^{\langle i\rangle} + k_{11}^{\langle i+1\rangle} & k_{34}^{\langle i\rangle} + k_{12}^{\langle i+1\rangle} \\ k_{41}^{\langle i\rangle} & k_{42}^{\langle i\rangle} & k_{43}^{\langle i\rangle} + k_{21}^{\langle i+1\rangle} & k_{44}^{\langle i\rangle} + k_{22}^{\langle i+1\rangle} \end{bmatrix}, \tag{10}$$

$$[M_G]_i = \begin{bmatrix} m_{33}^{\langle i-1\rangle} + m_{11}^{\langle i\rangle} + \Delta m_i & m_{34}^{\langle i-1\rangle} + m_{12}^{\langle i\rangle} & m_{13}^{\langle i\rangle} & m_{14}^{\langle i\rangle} \\ m_{43}^{\langle i\rangle} + m_{21}^{\langle i\rangle} & m_{44}^{\langle i\rangle} + m_{22}^{\langle i\rangle} & m_{23}^{\langle i\rangle} & m_{24}^{\langle i\rangle} \\ m_{31}^{\langle i\rangle} & m_{32}^{\langle i\rangle} & m_{33}^{\langle i\rangle} + m_{11}^{\langle i+1\rangle} & m_{34}^{\langle i\rangle} + m_{12}^{\langle i+1\rangle} \\ m_{41}^{\langle i\rangle} & m_{42}^{\langle i\rangle} & m_{43}^{\langle i\rangle} + m_{21}^{\langle i+1\rangle} & m_{44}^{\langle i\rangle} + m_{22}^{\langle i+1\rangle} \end{bmatrix}. \tag{11}$$

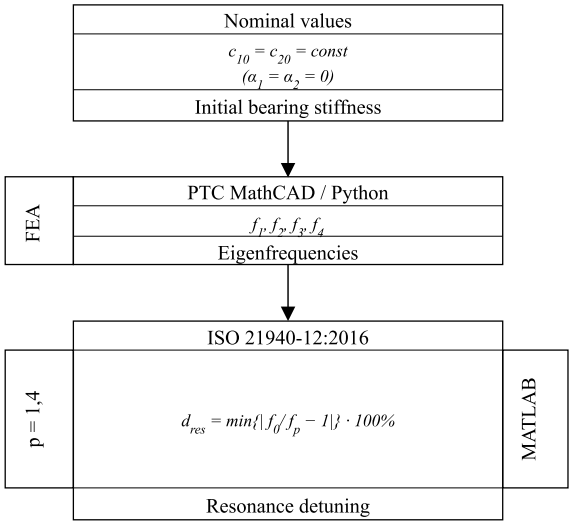


Fig. 2. Finite element analysis of rotor dynamics.

problem is solved numerically by finding positive roots ω_p (in ascending order) of the following algebraic equation:

$$\det\left([K_G(\omega_p)] - \omega_p^2[M_G]\right) = 0. \tag{14}$$

After considering the p-th eigenfrequency as $f_p = \omega_p/(2\pi)$ [Hz], an algorithm of the finite element analysis is presented in Fig. 2.

Data preparation is carried out in MS Excel. The auxiliary matrix calculations are performed using the MATLAB software.

Finally, in accordance with the international standard ISO 21940-12:2016, the resonance detuning can be evaluated as follows:

$$RD_p = \min_{p=\overline{1,4}} \left\{ \left| \frac{f_0}{f_p} - 1 \right| \right\} \cdot 100\%, \tag{15}$$

where f_0 is the operating frequency [Hz].

3.2. Linear evaluation of bearing stiffness using a modified Moore–Penrose pseudoinverse. In actual production conditions, the stiffness for each bearing support varies about its nominal value. Therefore, in a general case, $c_{10} \neq c_{20}$. Moreover, the stiffness depends on the rotor speed ($c_{10} \neq$ const, $c_{20} \neq$ const).

Considering both these facts, the actual bearing stiffnesses of the supports should be evaluated as follows:

$$c_1 = c_{10} + \alpha_1\omega, \quad c_2 = c_{20} + \alpha_2\omega, \tag{16}$$

where α_1, α_2 are unknown stiffness parameters [N·s/m] that should be evaluated together with the initial stiffnesses c_{10} and c_{20}.

For this purpose, the modified Moore–Penrose pseudoinverse can be applied using the actual critical frequencies. The corresponding algorithm is presented in Fig. 3.

Initially, bearing stiffness is evaluated using the linear matrix approach. For this purpose, according to the Monte Carlo method, an initial dataset of bearing stiffness parameters $c_{10}^{\langle j\rangle}$, $c_{20}^{\langle j\rangle}$, $\alpha_1^{\langle j\rangle}$, and $\alpha_2^{\langle j\rangle}$ is generated within a range from their minimum ($c_{\min}$ for $c_{10}^{\langle j\rangle}$ and $c_{20}^{\langle j\rangle}$, and 0 for $\alpha_1^{\langle j\rangle}$ and $\alpha_2^{\langle j\rangle}$) to maximum ($c_{\max}$ for $c_{10}^{\langle j\rangle}$ and $c_{20}^{\langle j\rangle}$, and $\alpha_{\max}$ for $\alpha_1^{\langle j\rangle}$ and $\alpha_2^{\langle j\rangle}$) values using a uniform distribution law:

$$\begin{aligned} c_{10}^{\langle j\rangle} &= c_{\min} + (c_{\max} - c_{\min}) \cdot \mathrm{rnd}(1), \\ c_{20}^{\langle j\rangle} &= c_{\min} + (c_{\max} - c_{\min}) \cdot \mathrm{rnd}(1), \end{aligned} \tag{17}$$

$$\begin{aligned} \alpha_1^{\langle j\rangle} &= \alpha_{\max} \cdot \mathrm{rnd}(1), \\ \alpha_2^{\langle j\rangle} &= \alpha_{\max} \cdot \mathrm{rnd}(1), \end{aligned} \tag{18}$$

where $\mathrm{rnd}(1)$ is a uniform distribution function in a range from 0 to 1.

Such an approach allows avoiding a significant amount of sample data, simultaneously ensuring a uniform distribution of values.

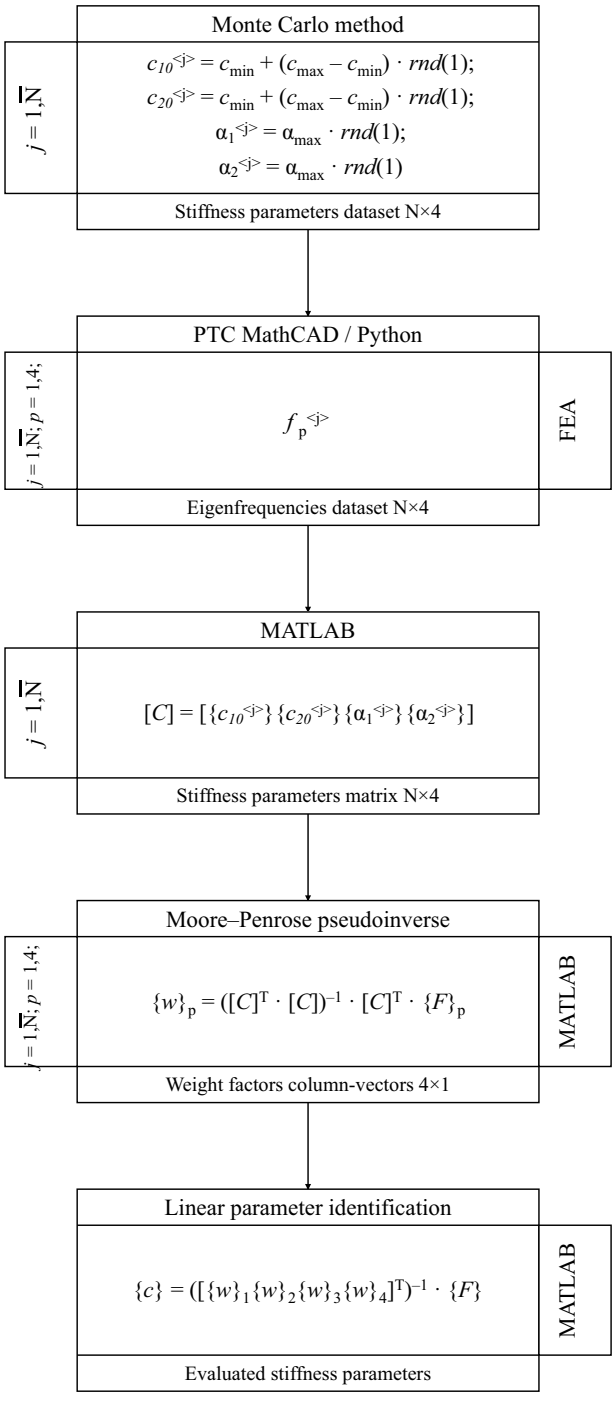


Fig. 3. Linear parameter identification using a modified Moore–Penrose pseudoinverse.

Next, a dataset of eigenfrequencies $f_p^{\langle j\rangle}$ is evaluated for each p-th mode shape within the j-th parameter set ($j = \overline{1,N}$). For this purpose, the authors' code (Pavlenko and Symonovskyi, 2015) of the computer algebra system PTC MathCAD 14 and the authors' code (Roshchupkin and Pavlenko, 2025) in the Python 3.13 programming

$i := 1 .. n \quad Nod_{i,1} := i \quad Nod_{i,2} := i + 1 \quad i := 1 .. 2 \cdot (n+1) \quad j := 1 .. 2 \cdot (n+1)$

$\underset{\sim}{K}_{i,j} := 0 \quad M_{i,j} := 0 \quad A_{i,j} := 0 \quad B_{i,j} := 0 \quad i := 1 .. n$

$K_{2 \cdot Nod_{i-1},\, 2 \cdot Nod_{i-1}} := K_{2 \cdot Nod_{i-1},\, 2 \cdot Nod_{i-1}} + \frac{12 \cdot E \cdot I_i}{(L_i)^3} + k_i$

$K_{2 \cdot Nod_{i-1},\, 2 \cdot Nod_i} := K_{2 \cdot Nod_{i-1},\, 2 \cdot Nod_i} + \frac{6 \cdot E \cdot I_i}{(L_i)^2}$

$K_{2 \cdot Nod_{i-1},\, 2 \cdot Nod_{i+1}} := K_{2 \cdot Nod_{i-1},\, 2 \cdot Nod_{i+1}} - \frac{12 \cdot E \cdot I_i}{(L_i)^3}$

$K_{2 \cdot Nod_{i-1},\, 2 \cdot Nod_{i+2}} := K_{2 \cdot Nod_{i-1},\, 2 \cdot Nod_{i+2}} + \frac{6 \cdot E \cdot I_i}{(L_i)^2}$

$K_{2 \cdot Nod_i,\, 2 \cdot Nod_{i-1}} := K_{2 \cdot Nod_i,\, 2 \cdot Nod_{i-1}} + \frac{6 \cdot E \cdot I_i}{(L_i)^2}$

$K_{2 \cdot Nod_i,\, 2 \cdot Nod_i} := K_{2 \cdot Nod_i,\, 2 \cdot Nod_i} + \frac{4 \cdot E \cdot I_i}{L_i}$

(a)

```
'''IMPORT MODULES'''

import pathlib, os.path, pandas as pd, numpy as np, math
from math import pi
from scipy import interpolate
import matplotlib.pyplot as plt

'''READ FILE'''

def getfile():
    while True:
        file = input('\nEnter file name *.xlsx: ')
        filename = file + '.xlsx'
        path = pathlib.Path(filename)
        if path.exists():
            return path
        else:
            print('Incorrect file name.')

file = getfile()

'''NUMBER OF EIGENFREQUENCIES'''

def getnumber():
    while True:
```

(b)

Fig. 4. Fragments of the PTC MathCAD file (a) and Python's programming code (b).

language (Fig. 4) are used.

Next, with a certain accuracy, the following linear dependency for the p-th eigenfrequency is proposed for at least $p = \overline{1,4}$:

$$f_p^{\langle j\rangle} = w_{j,1}\, c_{10}^{\langle j\rangle} + w_{j,2}\, c_{20}^{\langle j\rangle} + w_{j,3}\, \alpha_1^{\langle j\rangle} + w_{j,4}\, \alpha_2^{\langle j\rangle}. \quad (19)$$

It can also be written in a matrix form:

$$\{F\}_p = [C]\,\{w\}_p, \quad (20)$$

where $\{F\}_p = \{f_p^{\langle j\rangle}\}$ is the column-vector $N \times 1$ of p-th eigenfrequency values, $\{C\} = \{c_{10}^{\langle j\rangle}, c_{20}^{\langle j\rangle}, \alpha_1^{\langle j\rangle}, \alpha_2^{\langle j\rangle}\}$ denotes the matrix $N \times 4$ of stiffness parameters, and $\{w\}_p$ is the column-vector 4×1 of weight factors for the p-th eigenfrequency.

In a general case, when the total number of the dataset is more than that of stiffness parameters ($N > 4$), the column-vector 4×1 of the weight factors for the p-th eigenfrequency is determined according to the Moore–Penrose pseudoinverse:

$$\{w\}_p = \left([C]^T[C]\right)^{-1}[C]^T\{F\}_p. \tag{21}$$

The corresponding matrix calculations are performed using the MATLAB R2024b software.

For the entire range of p, the obtained column-vectors $\{w\}_p$ are augmented to the following generalized matrix 4×4 of weight factors $[\{w\}_1, \{w\}_2, \{w\}_3, \{w\}_4]$, which allows extending Eqn. (19) to the entire range of eigenfrequencies:

$$\{F\} = [\{w\}_1, \{w\}_2, \{w\}_3, \{w\}_4]^T\{c\}, \tag{22}$$

where $\{c\} = \{c_{10}, c_{20}, \alpha_1, \alpha_2\}^T$ is the column-vector 4×1 of the evaluated stiffness parameters that can be determined according to the inverse matrix approach:

$$\{c\} = \left([\{w\}_1, \{w\}_2, \{w\}_3, \{w\}_4]^T\right)^{-1}\{F\} \tag{23}$$

for the column-vector 4×1 of actual critical frequencies $\{F\} = \{f_1, f_2, f_3, f_4\}^T$, which can be obtained at a balancing stand.

The assumption of linearity in the dependence of eigenfrequencies on stiffness parameters limits the above-mentioned approach. However, in practice, such an assumption leads to a certain accuracy that should be eliminated using a nonlinear approach, e.g., artificial intelligence systems.

3.3. Nonlinear parameter identification using an artificial neural network. A nonlinear parameter identification approach is implemented using an artificial neural network, with its general architecture shown in Fig. 5.

It includes critical frequencies f_1, f_2, f_3, and f_4 as inlet parameters as well as stiffness parameters c_{10}, c_{20}, α_1, and α_2 as outlet parameters.

An algorithm of nonlinear parameter identification using an artificial neural network is presented in Fig. 6.

Initially, the Monte Carlo method is also applied according to the formulas (16) and (17). This allows the use of the exact dataset of previously generated eigenfrequencies.

Before processing, the ANN inputs and outputs are normalized to improve stability and learning speed and to obtain more accurate results.

The stiffness parameters can be normalized as follows:

$$\bar{c}_{10}^{\langle j\rangle} = \frac{c_{10}^{\langle j\rangle} - c_{\min}}{c_{\max} - c_{\min}}, \quad \bar{c}_{20}^{\langle j\rangle} = \frac{c_{20}^{\langle j\rangle} - c_{\min}}{c_{\max} - c_{\min}}, \tag{24}$$

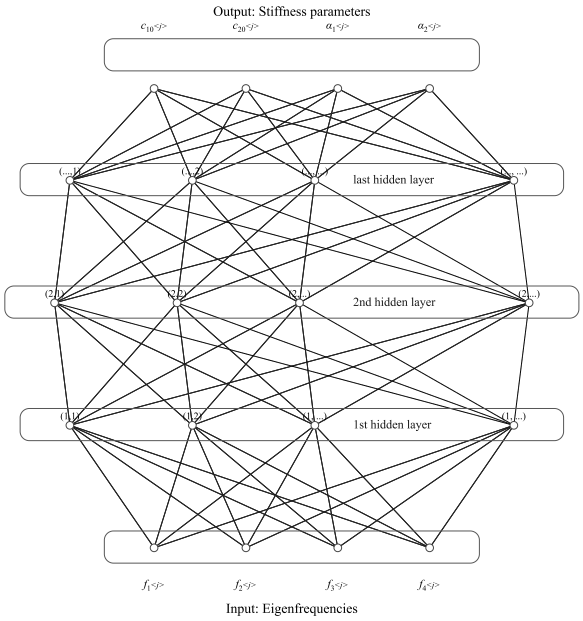


Fig. 5. General neural network architecture.

$$\bar{\alpha}_1^{\langle j\rangle} = \frac{\alpha_1^{\langle j\rangle}}{\alpha_{\max}}, \quad \bar{\alpha}_2^{\langle j\rangle} = \frac{\alpha_2^{\langle j\rangle}}{\alpha_{\max}}. \tag{25}$$

The eigenfrequencies can also be normalized as

$$\bar{f}_p^{\langle j\rangle} = \frac{f_p^{\langle j\rangle} - f_p^{\min}}{f_p^{\max} - f_p^{\min}}, \tag{26}$$

where $p = \overline{1,4}$ is the mode number while $f_p^{\min}$ and $f_p^{\max}$ are minimum and maximum values of the p-th eigenfrequency, obtained using the finite element analysis.

Such normalization avoids the dimensionality problem by providing the same scale for the system's input and output parameters. It also avoids the difficulties of changing gradients during backpropagation. A normalized model generalizes patterns better and is less prone to overfitting.

The training of the artificial neural network can be realized using the backpropagation approach with a proper choice of the learning rate, momentum coefficient, transfer function (e.g., hyperbolic tangent), maximum number of training cycles, target error, initialization method of threshold and weight factors (e.g., random), and analysis update interval.

During the learning process, the following parameters are varied for the j-th dataset: dimensionless eigenfrequencies $\bar{f}_1^{\langle j\rangle}$, $\bar{f}_2^{\langle j\rangle}$, $\bar{f}_3^{\langle j\rangle}$, and $\bar{f}_4^{\langle j\rangle}$ for inputs, as well as dimensionless stiffness parameters $\bar{c}_{10}^{\langle j\rangle}$, $\bar{c}_{20}^{\langle j\rangle}$, $\bar{\alpha}_1^{\langle j\rangle}$, and $\bar{\alpha}_2^{\langle j\rangle}$ for outputs.

The accuracy of parameter estimation is evaluated by the regression coefficient r^2 (which should approach

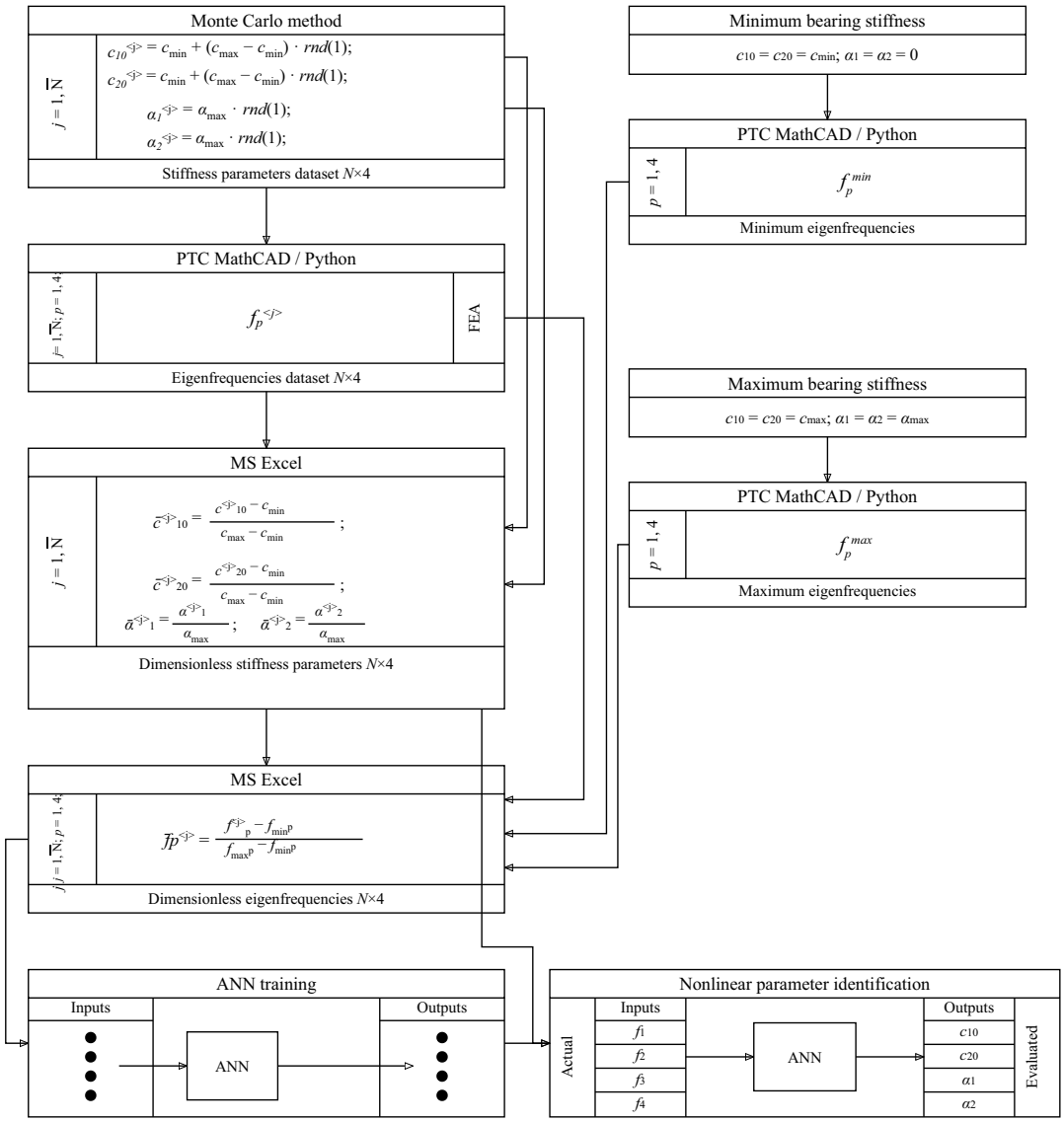


Fig. 6. Nonlinear parameter identification using an artificial neural network.

1), the slope coefficient (should also approach 1), and the y-intercept (which should approach 0).

The evaluated dimensionless stiffness parameters are obtained for the actual dimensionless critical frequencies. Finally, their dimensional values are calculated as follows:

$$\begin{aligned} c_{10} &= c_{\min} + (c_{\max} - c_{\min}) \cdot \bar{c}_{10}, \\ c_{20} &= c_{\min} + (c_{\max} - c_{\min}) \cdot \bar{c}_{20}, \end{aligned} \tag{27}$$

$$\alpha_1 = \alpha_{\max} \cdot \bar{\alpha}_1, \quad \alpha_2 = \alpha_{\max} \cdot \bar{\alpha}_2. \tag{28}$$

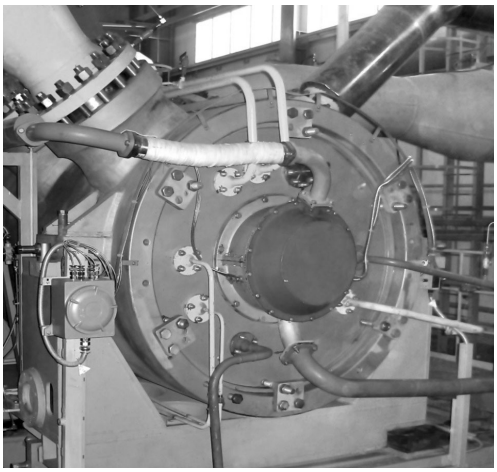
4. Results

4.1. Results of the finite element analysis. The finite element model was developed using the computer algebra system PTC MathCAD and the Python programming language to expand the computational methods for evaluating eigenfrequencies.

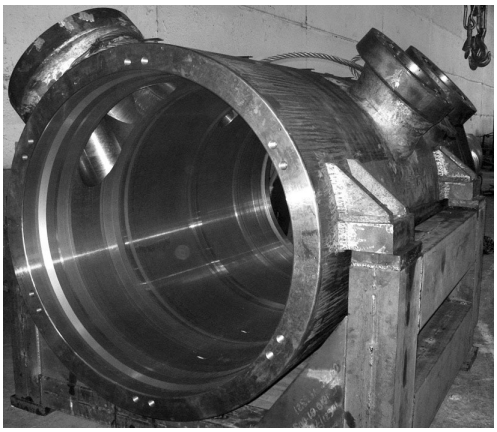
A multistage centrifugal compressor S325 GC2-650/6-56M12 case study was considered for the natural gas compressor station "Gazli" (Uzbekistan). This class of compressors is designed for a natural gas transportation system. The rotor is flexible because its operating speed exceeds the first (or even higher) critical speed.

The general view of the compressor, housing, and the rotor is presented in Fig. 7.

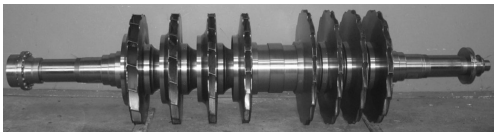
Technical characteristics of the compressors include flow performance reduced to a temperature of 273 K and a pressure of 0.1 MPa: 62.5 m^3/s, volumetric capacity reduced to initial conditions: 3.97 m^3/s, inlet



(a)



(b)



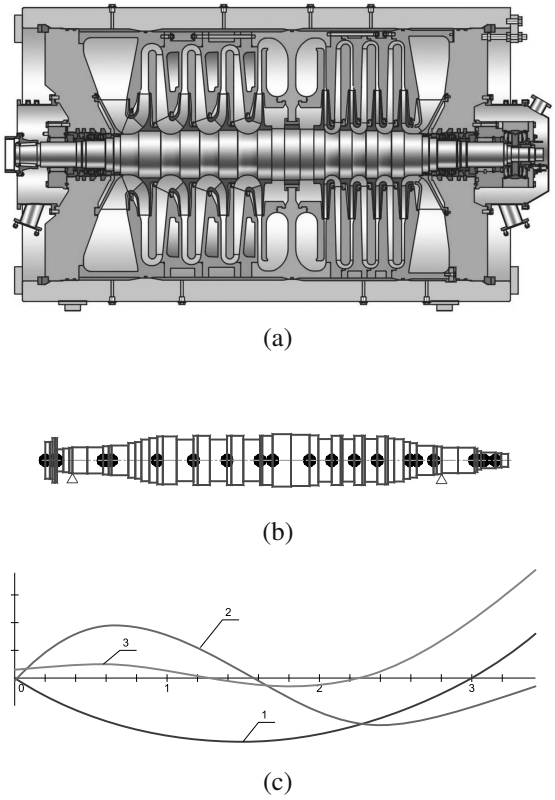
(c)

Fig. 7. Compressor S325 GC2-65 6/6 56M12: general view (a), housing (b), rotor (c).

temperature: 313.2 K, inlet absolute pressure: 0.59 MPa, temperature difference: 116.7 K, outlet absolute pressure: 5.57 MPa, pressure ratio: 9.4, polytropic energy efficiency: 71%, rotor speed: 7500 rpm (operating frequency $f_0 = 125$ Hz), nominal power consumption: 25 MW, compression ratio for the inlet conditions: 0.99.

Physical parameters of the rotor are the following: material is 1.5732 steel DIN/EN-14NiCr10, density $\rho = 7850$ kg/m^3, Young's modulus of elasticity $E = 2.1 \cdot 10^{11}$ N/m^2.

The following parameters were used to describe the



(a)

(b)

(c)

Fig. 8. Cross-section (a) and design scheme (b) of the centrifugal compressor, and mode shapes with eigenfrequencies (c) obtained for the nominal bearing stiffness using the PTC MathCAD computer algebra system: 1—1st mode, 2—2nd mode, 3—3rd mode (dots are added masses, triangles are bearing supports).

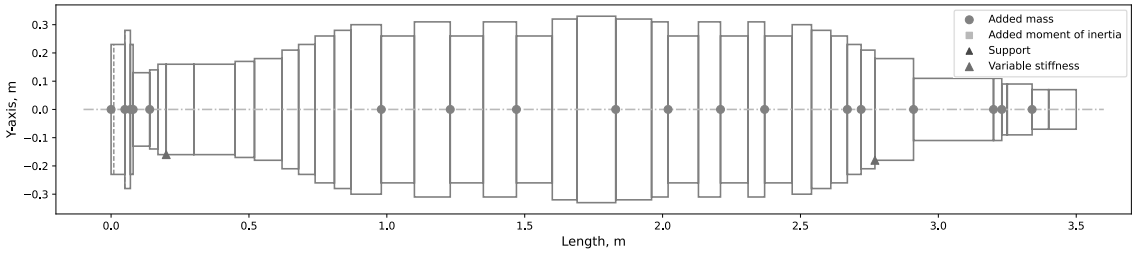
i-th section of the rotor in the finite element model: inner diameter D_i [m], outer diameter d_i [m], length of a shaft part l_i [m], m_i [kg].

Initially, nominal stiffness of bearings $c_{10} = c_{20} = 6 \cdot 10^8$ N/m is considered for the 8th and 49th shaft parts, respectively.

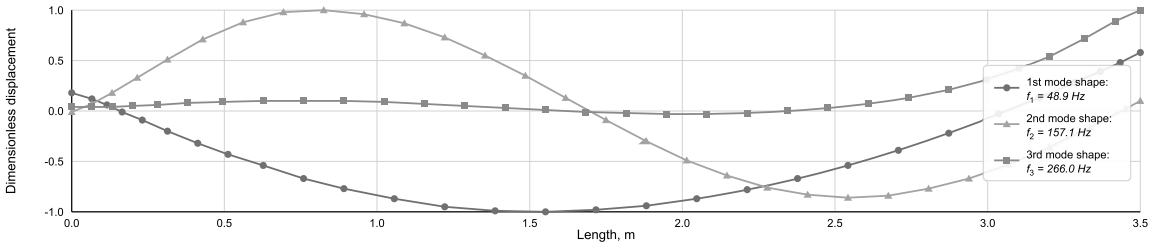
General initial data for the finite element model are summarized in Table 2.

A cross-section, the design scheme, and the evaluated eigenfrequencies and mode shapes obtained for the nominal bearing stiffness using the patented authors' program code realized in the PTC MathCAD computer algebra system are presented in Fig. 8. The same, using the authors' program code realized in the Python programming language, is also presented in Fig. 9.

The numerical results obtained for the first three eigenfrequencies are summarized in Table 3. The discrepancy in the results, ranging from 0.3% to 1.1% across modes, demonstrates the consistency of different software solutions in solving the eigenvalue problem.



(a)



(b)

```
EIGENFREQUENCIES, Hz:
---------------------
f[1] = 48.9
f[2] = 157.1
f[3] = 266.0

---------------------
MODE SHAPES:
---------------------
mode_shape[1] = [ 0.183 0.137 0.105 0.082 0.058 -0.019 -0.088 -0.122 -0.289 -0.454
 -0.502 -0.526 -0.649 -0.69 -0.723 -0.761 -0.798 -0.819 -0.876 -0.93
 -0.941 -0.97 -0.993 -0.996 -1. -0.99 -0.988 -0.971 -0.936 -0.887
 -0.861 -0.858 -0.812 -0.774 -0.766 -0.71 -0.668 -0.656 -0.586 -0.535
 -0.52 -0.483 -0.42 -0.378 -0.328 -0.199 -0.176 -0.132 0.002 0.137
  0.159 0.189 0.217 0.313 0.357 0.418]

mode_shape[2] = [-0.04 0.028 0.075 0.11 0.144 0.257 0.359 0.409 0.651 0.861
  0.91 0.932 1. 0.997 0.985 0.961 0.929 0.906 0.829 0.709
  0.676 0.561 0.394 0.348 0.217 0.023 0.005 -0.113 -0.305 -0.491
 -0.572 -0.579 -0.679 -0.738 -0.749 -0.807 -0.836 -0.842 -0.865 -0.87
 -0.87 -0.868 -0.856 -0.841 -0.817 -0.717 -0.696 -0.656 -0.54 -0.43
 -0.412 -0.388 -0.366 -0.292 -0.258 -0.211]

mode_shape[3] = [ 4.492e-02 4.877e-02 5.148e-02 5.341e-02 5.534e-02 6.191e-02
  6.814e-02 7.133e-02 8.739e-02 9.976e-02 1.017e-01 1.022e-01
  9.858e-02 9.367e-02 8.841e-02 8.092e-02 7.245e-02 6.693e-02
  5.050e-02 2.967e-02 2.457e-02 8.426e-03 -1.066e-02 -1.504e-02
 -2.627e-02 -3.764e-02 -3.830e-02 -4.165e-02 -4.355e-02 -4.043e-02
 -3.698e-02 -3.660e-02 -2.744e-02 -1.807e-02 -1.612e-02 -2.572e-04
  1.246e-02 1.603e-02 3.880e-02 5.628e-02 6.176e-02 7.492e-02
  9.817e-02 1.145e-01 1.359e-01 2.073e-01 2.230e-01 2.564e-01
  3.914e-01 5.630e-01 5.930e-01 6.349e-01 6.755e-01 8.262e-01
  8.991e-01 1.000e+00]
---------------------
Completed successfully.
```

(c)

Fig. 9. Design scheme (a), mode shapes with eigenfrequencies (b), and command prompt (c) obtained for the nominal bearing stiffness using the Python program code.

Table 2. General data for the finite element analysis.

i	D_i [m]	d_i [m]	l_i [m]	Δm_i [kg]	c_i [N/m]
1	0.030	0.227	0.198	18.0	–
2	0.021	0.227	0.206	–	–
3	0.015	0.275	0.206	2.5	–
4	0.015	0.275	0.188	2.5	–
5	0.050	0.133	–	12.0	–
6	0.045	0.139	–	–	–
7	0.022	0.152	–	–	–
8	0.110	0.160	–	–	$6 \cdot 10^8$
9	0.120	0.160	–	–	–
10	0.040	0.171	–	–	–
11	0.021	0.176	–	–	–
12	0.125	0.180	–	–	–
13	0.053	0.210	–	–	–
14	0.046	0.230	–	–	–
15	0.058	0.260	–	–	–
16	0.060	0.275	–	–	–
17	0.037	0.300	–	102.0	–
18	0.105	0.300	–	–	–
19	0.125	0.260	–	–	–
20	0.030	0.305	–	100.0	–
21	0.096	0.305	–	–	–
22	0.124	0.260	–	–	–
23	0.032	0.310	–	99.0	–
24	0.089	0.310	–	–	–
25	0.129	0.262	–	–	–
26	0.012	0.315	–	92.0	–
27	0.080	0.315	–	–	–
28	0.133	0.330	–	22.5	–
29	0.139	0.325	–	–	–
30	0.065	0.315	–	98.0	–
31	0.006	0.315	–	–	–
32	0.095	0.264	–	–	–
33	0.068	0.310	–	99.0	–
34	0.013	0.310	–	–	–
35	0.089	0.264	–	–	–
36	0.060	0.305	–	100.0	–
37	0.016	0.305	–	–	–
38	0.092	0.264	–	–	–
39	0.063	0.300	–	102.0	–
40	0.019	0.300	–	–	–
41	0.044	0.274	–	–	–
42	0.072	0.264	–	–	–
43	0.046	0.230	–	–	–
44	0.053	0.210	–	8.0	–
45	0.125	0.180	–	8.0	–
46	0.021	0.176	–	2.0	–
47	0.040	0.171	–	–	–
48	0.121	0.160	–	–	$6 \cdot 10^8$
49	0.122	0.160	–	–	–
50	0.020	0.140	–	1.5	–
51	0.027	0.110	–	–	–
52	0.025	0.092	–	15.0	–
53	0.086	0.091	–	4.2	–
54	0.040	0.090	–	1.3	–
55	0.055	0.080	–	–	–

Table 3. Comparison of the numerical simulation results.

Mode's number	PTC MathCAD	Python code	Relative error %
1	49.0	48.9	0.3
2	157.7	157.1	0.4
3	268.8	266.0	1.1

Table 4. Range of the parameter changes.

Parameter	Minimum	Nominal	Maximum
c_{10} [N/m]	$5 \cdot 10^8$	$6 \cdot 10^8$	$1 \cdot 10^9$
c_{20} [N/m]	$5 \cdot 10^8$	$6 \cdot 10^8$	$1 \cdot 10^9$
α_1 [N·s/m]	0	0	$1 \cdot 10^3$
α_2 [N·s/m]	0	0	$1 \cdot 10^3$

4.2. Regression analysis results. The operating frequency $f_0 = 125$ Hz between the first two eigenfrequencies proves the rotor's flexibility. The 2nd resonance detuning formula (15) equals 20%.

According to the international standard ISO 21940-12:2016, this demonstrates the boundary value of vibration reliability at a nominal operating mode with unchangeable bearing stiffnesses.

The final evaluation was realized using the available data about the actual first four critical frequencies $f_1 = 49.2$ Hz, $f_2 = 172.0$ Hz, $f_3 = 365.9$ Hz, and $f_4 = 437.3$ Hz, which were obtained at the accelerating-balancing stand "Schenck" with a vacuum chamber (JSC "SMNPO Engineering").

According to the Monte Carlo method, the stiffness parameters c_{10}, c_{20}, α_1, and α_2 are randomly varied within their reliable ranges using the uniform distribution law presented in Table 4.

A resulting set of $N = 50$ randomly generated parameters is summarized in Table 5.

Using the above-mentioned finite element analysis via Python, a dataset of critical frequencies was calculated for each randomly generated dataset $j = 1, 2, \ldots, N$ and summarized in Table 6.

Variations of these four frequencies range from 3 to 38% depending on the mode shape number. This fact additionally indicates the importance of parameter identification, based on Eqn. (16). As a result, the column vectors of weight factors were obtained using the modified Moore–Penrose pseudoinverse (21) and summarized in Table 7.

Finally, for the case of the column-vector of actual critical frequencies $\{F\} = \{49.2,\ 172.0,\ 365.9,\ 437.3\}^T$, the matrix of weight factors (Table 7) allows evaluating the stiffness parameters: $c_{10} = 6.25 \cdot 10^8$ N/m, $c_{20} = 5.76 \cdot 10^8$ N/m, $\alpha_1 = 628$ N·s/m, $\alpha_2 = 239$ N·s/m.

The calculated values of the eigenfrequencies are shown in Fig. 10 and summarized in Table 8.

Thus, linear parameter identification allows

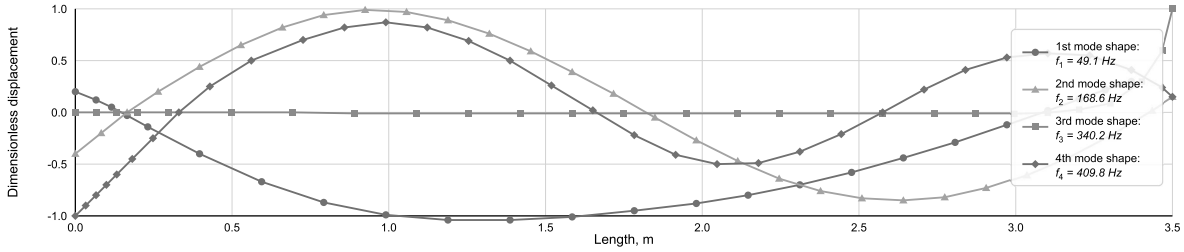


Fig. 10. Mode shapes for eigenfrequencies obtained for the evaluated bearing stiffness parameters using the modified Moore–Penrose pseudoinverse.

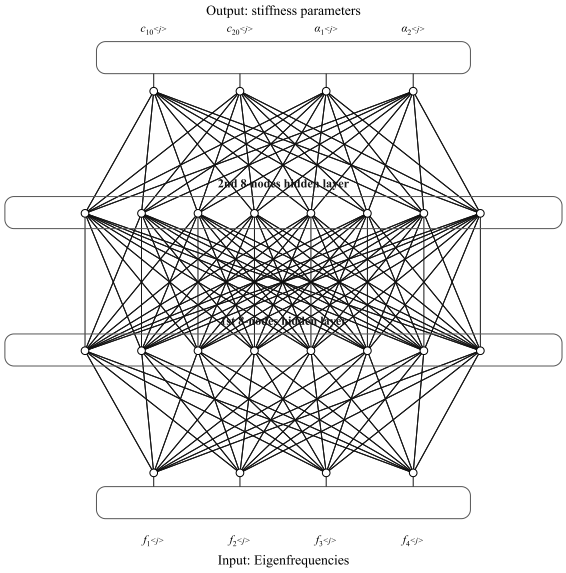


Fig. 11. General neural network architecture.

evaluation of the parameters corresponding to the first two frequencies.

However, the nonlinear approach based on artificial neural networks is needed to extend this precision to higher-order mode shapes.

4.3. Artificial intelligence results. The Visual Gene Developer 2.1 software was used to solve an inverse problem in the nonlinear identification of bearing stiffness parameters. The neural network architecture is presented in Fig. 11.

Its configuration parameters are as follows: the number of input variables is 4 (eigenfrequencies presented in Table 6), that of output parameters is 4 (stiffness parameters presented in Table 5), that of hidden layers is 2, the node number of the 1st hidden layer is 8, and the number of nodes of the 2nd hidden layer is 8.

Before processing, the output parameters were normalized by Eqns. (24) and (25), where minimum and maximum values of the stiffness parameters correspond to the data presented in Table 4: $c_{\min} = 5 \cdot 10^8$ N/m, $c_{\max} = 1 \cdot 10^9$ N/m, $\alpha_{\max} = 1 \cdot 10^3$ N·s/m.

The input parameters were also normalized using Eqn. (26), where the maximum eigenfrequencies were obtained via finite element analysis for the maximum stiffness $c_{10} = c_{20} = c_{\max} = 1 \cdot 10^9$ N/m, which can be adjusted by the parameters $\alpha_1 = \alpha_2 = \alpha_{\max} = 1 \cdot 10^3$ N·s/m.

The minimum and maximum eigenfrequencies are summarized in Table 9.

Variations in these frequencies range from 5 to 39% compared with the dataset presented in Table 9, which proves the proper choice of the total number $N = 50$ of the generated dataset.

Normalized datasets of input and output parameters are presented in Tables 10 and 11, respectively.

Considering that the data sets were randomly generated, the substantiation of such a dataset can be focused on the statistical error, i.e., the following approximation accuracy:

$$\epsilon = \frac{\sigma_{out}}{\sqrt{N}}, \tag{29}$$

where σ_{out} is the standard deviation of the output data.

In particular, based on the randomly generated data, summarized in Tables 10–11, σ_{out} ranges from 0.169 to 0.273 depending on the frequency. Therefore, according to the formula (29), the mean-square error ϵ is in the range of 0.024–0.039 (Fig. 12).

For training the artificial neural network, the settings included learning rate: 0.001, momentum coefficient of 0.01, transfer function: a hyperbolic tangent, maximum number of training cycles: $1.2 \cdot 10^6$, target error of $1 \cdot 10^{-5}$, initialization method of thresholds: random, initialization method of weight factors: random, analysis update interval: 500 cycles.

An ANN map analysis of the weight factors allows proving the rational choice of the ANN architecture (Fig. 13).

Notably, an ANN architecture with a larger number of hidden layers and neurons in each was chosen. Afterward, the ANN map analysis showed that not

Table 5. Randomly generated dataset.

j	$c_{10}^{\langle j\rangle}$	$c_{20}^{\langle j\rangle}$	$\alpha_1^{\langle j\rangle}$	$\alpha_2^{\langle j\rangle}$
1	$9.27 \cdot 10^8$	$6.66 \cdot 10^8$	735	9
2	$5.28 \cdot 10^8$	$5.19 \cdot 10^8$	726	462
3	$5.03 \cdot 10^8$	$5.29 \cdot 10^8$	285	806
4	$5.85 \cdot 10^8$	$6.93 \cdot 10^8$	345	170
5	$9.36 \cdot 10^8$	$9.16 \cdot 10^8$	252	7
6	$7.29 \cdot 10^8$	$9.54 \cdot 10^8$	159	336
7	$6.02 \cdot 10^8$	$6.32 \cdot 10^8$	889	527
8	$8.12 \cdot 10^8$	$7.97 \cdot 10^8$	502	677
9	$5.18 \cdot 10^8$	$8.54 \cdot 10^8$	242	44
10	$6.06 \cdot 10^8$	$8.97 \cdot 10^8$	359	711
11	$6.72 \cdot 10^8$	$7.63 \cdot 10^8$	338	322
12	$9.65 \cdot 10^8$	$5.05 \cdot 10^8$	566	128
13	$5.19 \cdot 10^8$	$6.19 \cdot 10^8$	680	5
14	$8.44 \cdot 10^8$	$9.46 \cdot 10^8$	408	181
15	$9.60 \cdot 10^8$	$7.91 \cdot 10^8$	51	969
16	$8.35 \cdot 10^8$	$5.87 \cdot 10^8$	316	213
17	$5.46 \cdot 10^8$	$7.12 \cdot 10^8$	65	51
18	$7.17 \cdot 10^8$	$6.41 \cdot 10^8$	382	969
19	$8.46 \cdot 10^8$	$7.20 \cdot 10^8$	846	455
20	$6.75 \cdot 10^8$	$7.69 \cdot 10^8$	955	81
21	$6.87 \cdot 10^8$	$7.38 \cdot 10^8$	597	514
22	$5.03 \cdot 10^8$	$8.71 \cdot 10^8$	611	136
23	$8.61 \cdot 10^8$	$6.22 \cdot 10^8$	178	502
24	$5.31 \cdot 10^8$	$5.27 \cdot 10^8$	642	565
25	$8.47 \cdot 10^8$	$5.60 \cdot 10^8$	305	185
26	$7.64 \cdot 10^8$	$7.54 \cdot 10^8$	380	763
27	$7.97 \cdot 10^8$	$9.75 \cdot 10^8$	8	63
28	$8.72 \cdot 10^8$	$7.02 \cdot 10^8$	101	440
29	$9.40 \cdot 10^8$	$5.22 \cdot 10^8$	878	73
30	$7.35 \cdot 10^8$	$5.33 \cdot 10^8$	551	343
31	$7.77 \cdot 10^8$	$7.57 \cdot 10^8$	859	688
32	$9.08 \cdot 10^8$	$6.53 \cdot 10^8$	180	875
33	$5.65 \cdot 10^8$	$6.71 \cdot 10^8$	366	683
34	$6.34 \cdot 10^8$	$8.26 \cdot 10^8$	89	22
35	$6.89 \cdot 10^8$	$6.14 \cdot 10^8$	951	734
36	$7.88 \cdot 10^8$	$8.35 \cdot 10^8$	726	913
37	$5.29 \cdot 10^8$	$6.29 \cdot 10^8$	276	166
38	$8.63 \cdot 10^8$	$8.60 \cdot 10^8$	898	963
39	$6.44 \cdot 10^8$	$7.01 \cdot 10^8$	584	508
40	$8.68 \cdot 10^8$	$7.39 \cdot 10^8$	993	680
41	$5.47 \cdot 10^8$	$9.93 \cdot 10^8$	652	652
42	$6.68 \cdot 10^8$	$6.45 \cdot 10^8$	778	339
43	$6.50 \cdot 10^8$	$8.79 \cdot 10^8$	631	233
44	$6.19 \cdot 10^8$	$7.82 \cdot 10^8$	224	937
45	$6.27 \cdot 10^8$	$6.67 \cdot 10^8$	67	580
46	$5.44 \cdot 10^8$	$5.20 \cdot 10^8$	419	953
47	$7.82 \cdot 10^8$	$6.03 \cdot 10^8$	24	6
48	$9.39 \cdot 10^8$	$9.45 \cdot 10^8$	756	574
49	$5.50 \cdot 10^8$	$7.54 \cdot 10^8$	191	331
50	$9.67 \cdot 10^8$	$9.31 \cdot 10^8$	377	99

Table 6. Calculated eigenfrequencies.

j	$f_1^{\langle j\rangle}$	$f_2^{\langle j\rangle}$	$f_3^{\langle j\rangle}$	$f_4^{\langle j\rangle}$
1	49.8	165.2	277.4	392.4
2	48.8	172.1	365.8	437.5
3	48.7	173.0	373.5	460.9
4	49.3	167.8	329.3	403.5
5	50.3	169.7	298.7	393.7
6	50.0	172.8	362.9	429.6
7	49.4	175.0	369.3	445.0
8	50.1	176.7	372.9	456.4
9	49.3	166.8	304.3	394.9
10	49.8	175.8	373.4	458.7
11	49.7	171.8	359.1	424.5
12	49.3	163.8	300.4	397.5
13	48.9	162.3	271.5	391.9
14	50.2	173.1	344.8	409.4
15	50.2	176.4	373.9	462.4
16	49.5	167.7	334.4	406.6
17	49.1	162.1	293.6	384.0
18	49.6	176.7	375.1	466.9
19	50.0	175.4	367.3	439.5
20	49.7	169.9	308.6	397.3
21	49.7	175.0	369.4	445.1
22	49.4	171.2	331.2	403.1
23	49.7	172.6	368.0	442.7
24	48.8	173.3	369.8	447.1
25	49.4	166.3	324.5	403.0
26	49.9	176.3	373.7	460.2
27	50.1	169.0	318.5	378.8
28	49.9	172.2	365.8	437.6
29	49.3	162.6	282.9	394.3
30	49.2	170.2	356.6	423.1
31	50.0	177.5	373.0	456.7
32	49.9	176.0	374.2	464.0
33	49.3	174.2	372.5	455.9
34	49.6	165.3	295.2	390.6
35	49.6	177.1	373.3	458.2
36	50.1	178.7	375.2	465.9
37	48.9	165.4	323.8	401.9
38	50.3	179.5	375.6	467.4
39	49.6	174.5	369.0	444.2
40	50.1	177.8	372.9	456.2
41	49.8	177.2	373.1	456.4
42	49.5	172.4	358.6	424.7
43	49.9	173.3	351.2	414.9
44	49.6	175.3	374.7	466.3
45	49.3	170.7	368.3	433.2
46	48.9	175.5	374.9	466.0
47	49.3	159.6	269.2	381.8
48	50.4	177.8	371.8	451.5
49	49.3	169.6	359.6	425.4
50	50.3	172.1	325.3	400.4

Table 7. Elements of the matrix of weight factors.

No.	$\{w\}_1$	$\{w\}_2$	$\{w\}_3$	$\{w\}_4$
1	$2.7 \cdot 10^{-8}$	$8.3 \cdot 10^{-8}$	$1.4 \cdot 10^{-7}$	$2.0 \cdot 10^{-7}$
2	$3.4 \cdot 10^{-8}$	$1.2 \cdot 10^{-7}$	$2.4 \cdot 10^{-7}$	$2.7 \cdot 10^{-7}$
3	$5.7 \cdot 10^{-2}$	$2.3 \cdot 10^{-2}$	$4.1 \cdot 10^{-2}$	$5.6 \cdot 10^{-2}$
4	$4.4 \cdot 10^{-3}$	$2.7 \cdot 10^{-2}$	$1.2 \cdot 10^{-1}$	$1.2 \cdot 10^{-1}$

Table 8. Analysis of the data evaluated by ML.

Parameter	Mode 1	Mode 2	Mode 3	Mode 4
Actual	49.2	172.0	365.9	437.3
Evaluated	49.1	168.6	340.2	409.8
Error [%]	0.2	2.0	7.0	6.3

Table 9. Limits of the evaluated eigenfrequencies.

Mode shape p	Minimum $f_p^{\min}$ [Hz]	Nominal f_p [Hz]	Maximum $f_p^{\max}$ [Hz]
1	48.2	49.2	50.6
2	151.1	172.0	180.4
3	254.2	365.9	375.9
4	321.9	437.3	468.8

all groups of neurons were involved, as many links with a zero-weights remained. After removing these "extra" neurons step by step, the ANN architecture was rationalized, as shown in Fig. 13.

The resulting ANN map demonstrates weighted connections of a multilayer structure, which reflects the structure (four inputs, four outputs, two hidden layers with eight neurons in each), sign (negative, zero, and positive), and relative magnitude of connections (thickness of the links) between neurons of adjacent layers.

The network has a multilayer feed-forward architecture with clearly presented input, hidden, and output layers. Each neuron is connected to all neurons in the next layer, resulting in a fully connected topology.

The color of the link corresponds to the sign of the weight: dark gray—negative weights, light gray—positive weights. The thickness of the lines reflects the modulus of the weight: thick lines stand for strong influence while thin ones for influence.

The heterogeneous nature of the weight distribution is observed: not all inputs affect the outputs equally—some paths are clearly dominant. The lack of regular symmetry indicates that the ANN has learned nonlinear relationships rather than just linear transformations.

The presence of both positive and negative strong weights indicates correct learning, and the absence of "useless" neurons. Also, the distribution of weights, without sharp concentrations at a single node, means a stable learning process.

Table 10. Normalized eigenfrequencies.

j	$\bar{f}_1^{\langle j \rangle}$	$\bar{f}_2^{\langle j \rangle}$	$\bar{f}_3^{\langle j \rangle}$	$\bar{f}_4^{\langle j \rangle}$
1	0.667	0.481	0.191	0.480
2	0.250	0.717	0.917	0.787
3	0.208	0.747	0.980	0.946
4	0.458	0.570	0.617	0.555
5	0.875	0.635	0.366	0.489
6	0.750	0.741	0.893	0.733
7	0.500	0.816	0.946	0.838
8	0.792	0.874	0.975	0.916
9	0.458	0.536	0.412	0.497
10	0.667	0.843	0.979	0.931
11	0.625	0.706	0.862	0.698
12	0.458	0.433	0.380	0.515
13	0.292	0.382	0.142	0.477
14	0.833	0.751	0.744	0.596
15	0.833	0.863	0.984	0.956
16	0.542	0.567	0.659	0.577
17	0.375	0.375	0.324	0.423
18	0.583	0.874	0.993	0.987
19	0.750	0.829	0.929	0.801
20	0.625	0.642	0.447	0.513
21	0.625	0.816	0.947	0.839
22	0.500	0.686	0.633	0.553
23	0.625	0.734	0.935	0.822
24	0.250	0.758	0.950	0.852
25	0.500	0.519	0.578	0.552
26	0.708	0.860	0.982	0.941
27	0.792	0.611	0.528	0.387
28	0.708	0.720	0.917	0.788
29	0.458	0.392	0.236	0.493
30	0.417	0.652	0.841	0.689
31	0.750	0.901	0.976	0.918
32	0.708	0.850	0.986	0.967
33	0.458	0.788	0.972	0.912
34	0.583	0.485	0.337	0.468
35	0.583	0.887	0.979	0.928
36	0.792	0.942	0.994	0.980
37	0.292	0.488	0.572	0.545
38	0.875	0.969	0.998	0.990
39	0.583	0.799	0.943	0.833
40	0.792	0.911	0.975	0.914
41	0.667	0.891	0.977	0.916
42	0.542	0.727	0.858	0.700
43	0.708	0.758	0.797	0.633
44	0.583	0.826	0.990	0.983
45	0.458	0.669	0.938	0.758
46	0.292	0.833	0.992	0.981
47	0.458	0.290	0.123	0.408
48	0.917	0.911	0.966	0.882
49	0.458	0.631	0.866	0.705
50	0.875	0.717	0.584	0.534

Table 11. Normalized stiffness parameters.

j	$\bar{c}_{10}^{\langle j\rangle}$	$\bar{c}_{20}^{\langle j\rangle}$	$\bar{\alpha}_1^{\langle j\rangle}$	$\bar{\alpha}_2^{\langle j\rangle}$
1	0.853	0.331	0.735	0.009
2	0.056	0.038	0.726	0.462
3	0.006	0.057	0.285	0.806
4	0.169	0.385	0.345	0.170
5	0.871	0.832	0.252	0.007
6	0.458	0.908	0.159	0.336
7	0.204	0.264	0.889	0.527
8	0.624	0.593	0.502	0.677
9	0.035	0.707	0.242	0.044
10	0.212	0.793	0.359	0.711
11	0.343	0.526	0.338	0.322
12	0.930	0.010	0.566	0.128
13	0.038	0.237	0.680	0.005
14	0.688	0.892	0.408	0.181
15	0.919	0.582	0.051	0.969
16	0.669	0.174	0.316	0.213
17	0.091	0.423	0.065	0.051
18	0.434	0.281	0.382	0.969
19	0.691	0.440	0.846	0.455
20	0.349	0.537	0.955	0.081
21	0.373	0.475	0.597	0.514
22	0.006	0.741	0.611	0.136
23	0.722	0.244	0.178	0.502
24	0.061	0.053	0.642	0.565
25	0.694	0.120	0.305	0.185
26	0.527	0.507	0.380	0.763
27	0.593	0.950	0.008	0.063
28	0.743	0.403	0.101	0.440
29	0.879	0.043	0.878	0.073
30	0.470	0.066	0.551	0.343
31	0.553	0.514	0.859	0.688
32	0.816	0.306	0.180	0.875
33	0.129	0.342	0.366	0.683
34	0.268	0.651	0.089	0.022
35	0.377	0.227	0.951	0.734
36	0.575	0.669	0.726	0.913
37	0.057	0.258	0.276	0.166
38	0.726	0.720	0.898	0.963
39	0.287	0.402	0.584	0.508
40	0.735	0.477	0.993	0.680
41	0.093	0.986	0.652	0.652
42	0.336	0.290	0.778	0.339
43	0.299	0.758	0.631	0.233
44	0.237	0.564	0.224	0.937
45	0.254	0.333	0.067	0.580
46	0.088	0.040	0.419	0.953
47	0.564	0.205	0.024	0.006
48	0.878	0.889	0.756	0.574
49	0.100	0.507	0.191	0.331
50	0.934	0.861	0.377	0.099

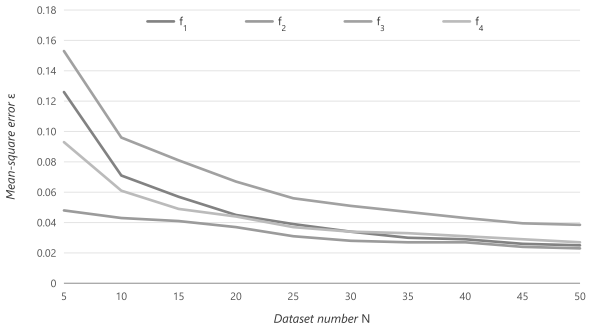


Fig. 12. Uncertainty quantification analysis.

Table 12. Statistical performance metrics of the ANN.

Metric	c_1	c_2	α_1	α_2
r^2	0.964	0.953	0.967	0.977
Slope	0.963	0.950	0.941	0.974
y-Intercept	0.024	0.012	0.033	0.013

Table 13. Robustness analysis data.

Parameter	Mode 1	Mode 2	Mode 3	Mode 4
$\mu_{MSE}^{\langle i\rangle}$	0.590	0.708	0.762	0.732
$\sigma_{MSE}^{\langle i\rangle}$	0.026	0.024	0.039	0.028
CV_i	0.044	0.034	0.050	0.038

As a result of training during the processing time of 1 h 2 min 50 s (Fig. 14), the following parameters were achieved: sum of error of 0.59, average error per output per dataset of $2.97 \cdot 10^{-3}$.

For predicting the stiffness parameters, the following regression analysis results (Fig. 15) were obtained: regression coefficient $r^2 = 0.953$–0.977, slope coefficient of 0.941–0.974, y-intercept of 0.012–0.033. The corresponding data is summarized in Table 12.

The robustness of the approach applied can be proven by the criteria of weights initialization as follows:

$$CV_i = \frac{\sigma_{MSE}^{\langle i\rangle}}{\mu_{MSE}^{\langle i\rangle}}, \tag{30}$$

where CV_i is the coefficient of variation for the sample within the evaluation of the i-th frequency while $\mu_{MSE}^{\langle i\rangle}$, $\sigma_{MSE}^{\langle i\rangle}$ are the mean value and standard deviation for the i-th sample. The data is summarized in Table 13.

Since the CV_i is within the range of 0.034–0.050 and does not exceed the critical value $CV_{cr} = 0.05$–0.10, the model is robust.

Finally, for the actual dimensionless critical frequencies $\bar{f}_1 = 0.417$, $\bar{f}_2 = 0.713$, $\bar{f}_3 = 0.918$, and $\bar{f}_4 = 0.786$, the artificial neural network allowed evaluating the following normalized outputs: $\bar{c}_{10} = 0.231$, $\bar{c}_{20} = 0.124$, $\bar{\alpha}_1 = 0.706$, and $\bar{\alpha}_2 = 0.339$.

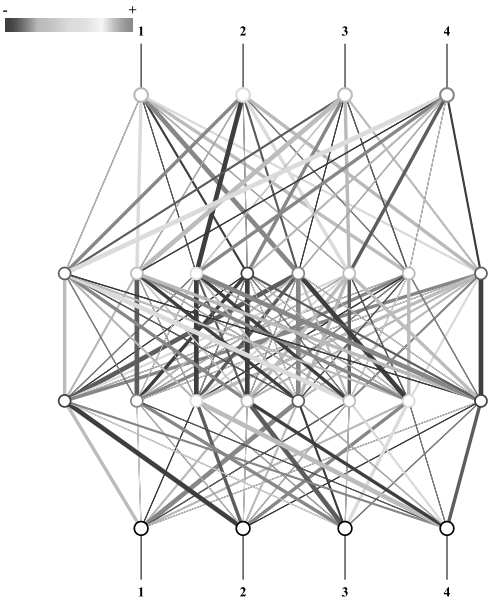


Fig. 13. ANN map analysis.

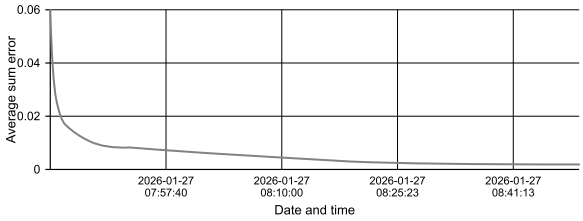


Fig. 14. Training error.

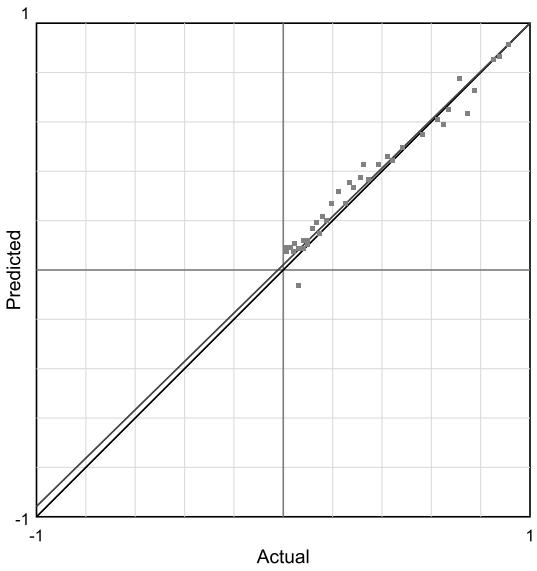


Fig. 15. Regression analysis.

According to Eqns. (27) and (28), these values correspond to the following stiffness parameters: $c_{10} = 6.16 \cdot 10^8$ N/m, $c_{20} = 5.62 \cdot 10^8$ N/m, $\alpha_1 = 706$ N·s/m, $\alpha_2 = 339$ N·s/m.

The calculated eigenfrequencies are shown in Fig. 16 and summarized in Table 14.

Thus, nonlinear parameter identification enables more precise parameter evaluation. In particular, the relative error of the second critical frequency has decreased from 2.0% to 0.7%.

5. Discussion

To analyze the strengths and drawbacks of the proposed methodology and the obtained results, potential challenges in studying rotor dynamics using artificial neural networks can be discussed, e.g., model accuracy, interpretability improvement, and overfitting prevention.

First, the model's accuracy depends on the amount of training data. A Monte Carlo method was applied to address this problem and improve the completeness of the training data. This allowed avoiding a significant amount of sample data, simultaneously ensuring a uniform distribution of the training dataset (Table 5) according to Eqn. (17). The data normalization equations (24)–(26) were also applied before processing to avoid problems with dimensionality and overfitting.

Second, a lack of interpretability is a common disadvantage because it makes the model operate as a "black box". However, the proposed approach is based on comprehensive use of the analytical dependence of bearing stiffness on rotor speed and on further application of numerical simulations via a free Python programming code, which enabled the realization of finite element modeling for an actual compressor S325 GC2-650/6-56M12 case study. Moreover, initial linear parameter identification with an artificial neural network was performed before applying nonlinear parameter identification using the Moore–Penrose pseudoinverse. Such an approach allowed determining the matrix of weight factors (Table 7) and employing it for further nonlinear analysis using the Visual Gene Developer 2.1 software.

Third, overfitting the training data can occur. To avoid this problem, the architecture was rationalized by reducing the number of hidden layers to two and the total number of neurons to 16 when all synaptic connections (Figure 13) were involved (absence of close-to-zero weight factors).

Significantly, the proposed FEM formulation is not restricted to linear stiffness and allows incorporating arbitrary functional dependencies, which are subsequently captured and refined using ANN-based correction. Furthermore, it should be noted that non-isotropic stiffness of the bearings is not allowed, as this leads to

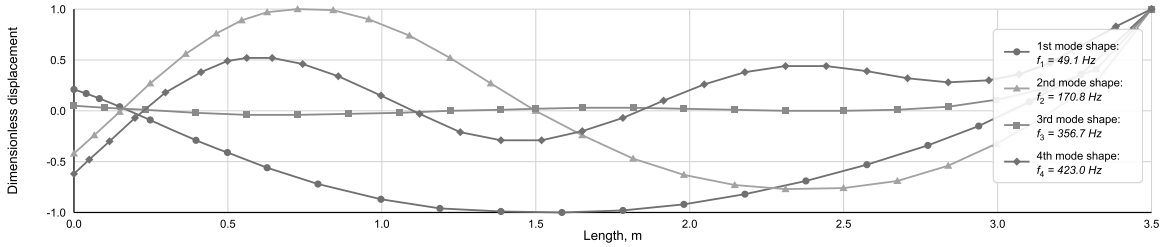


Fig. 16. Mode shapes for eigenfrequencies obtained for the evaluated bearing stiffness parameters using the artificial neural network.

Table 14. Analysis of the nonlinearly evaluated data.

Parameter	Mode 1	Mode 2	Mode 3	Mode 4
Actual*	49.2	172.0	365.9	437.3
Monte Carl-based sweep	49.5	167.7	334.4	406.6
Error [%]	0.6	2.5	8.6	7.0
ML(Moore–Penrose)	49.1	168.6	340.2	409.8
Error [%]	0.2	2.0	7.0	6.3
ANN	49.1	170.8	356.7	423.0
Error [%]	0.2	0.7	2.5	3.3

The symbol * corresponds to the data from the accelerating-balancing stand "Schenck" with a vacuum chamber (JSC "SMNPO Engineering").

the loss of dynamic stability of the circular precession of the shaft at frequencies close to twice the first critical frequency.

By implementing the proposed approach, the aforementioned challenges were mitigated, yielding more accurate, efficient, and interpretable results. Compared with the linear regression approach, which yielded relative errors in evaluating initial bearing stiffness of up to 7% (Table 8), the nonlinear parameter identification using the artificial neural network reduced this value by two-–three times (Table 13), depending on the mode shape.

The reliability of the developed models was also proven within realization of the R&D projects *Research on the Dynamics of Rotors of Turbopump Units and Reciprocating Compressor Units* (Ministry of Education and Science of Ukraine, grant no. 0117U004922) and *Conducting Research on the Dynamics of Rotors for Turbopump Units of Liquid Rocket Engines* (State Enterprise *Design Bureau Pivdenne named after M.K. Jangel*, grant no. 51.24-01.15.SP).

Despite ANN-based rotor diagnostics being reported in the literature, traditional approaches (Suryawanshi *et al*., 2025) address only a direct problem in which stiffnesses are the inputs and frequencies are the outputs. However, the problem is that the known models for direct calculation of bearing stiffness, based on geometric and physical parameters (e.g., Makivskyi *et al*., 2024; Zahorulko *et al*., 2023), are quite inaccurate. Moreover, such a direct approach does not allow further extension of the mathematical models of bearing stiffness. Despite this, our approach proposes estimating the bearing stiffness parameters (not only constants but also dependence coefficients) from actual data using an FEM-trained ANN to solve the inverse problem, with frequencies as inputs and the unknown bearing stiffness coefficients as outputs.

Notably, damping also plays a significant role in rotor vibration amplitudes and stability margins. As discussed in classical rotor dynamics studies (Zhang *et al*., 2020), stiffness-related effects are often the primary drivers of instability onset, while damping mainly affects the growth rate and steady-state response. In the present study, damping was intentionally neglected to isolate stiffness-induced instability mechanisms and critical speed shifts. The proposed FEM–ANN framework can be readily extended to include damping matrices for further studying forced oscillations and dynamic stability margins.

Also, future studies will aim to extend the parameter evaluation based on the amplitudes of forced oscillations, represented in the time and frequency domains. This will allow clarifying the damping ratio based on long-term compressor monitoring.

6. Conclusions

During the presented research, an approach was proposed to ensure the vibration reliability of rotary machines by more precisely evaluating bearing stiffness for reliable resonance detuning. As a result, a finite element model

of rotor dynamics was improved and realized in both the computer algebra system PTC MathCAD 14 and the programming language Python 3.13 using the authors' program codes. The discrepancy between the numerical simulation results does not exceed 1.1%.

Afterwards, a modified Moore–Penrose pseudo-inverse was applied using MATLAB to evaluate the stiffness parameters of bearing supports depending on the rotor speed.

Finally, an artificial neural network was architected using the Visual Gene Developer software to clarify the evaluated stiffness parameters in a nonlinear formulation with an accuracy of 0.2–0.7% for the first two critical frequencies.

The scientific novelty of the research lies in developing a hybrid parametric identification approach that leverages analytical dependencies in rotor dynamics, numerical finite element modeling of bearing stiffness as a function of rotor speed, and artificial neural networks to ensure vibration reliability in energy-intensive rotary machines.

The practical significance of the obtained results lies in their application to the design of an 8-stage centrifugal compressor S325 GC2-650/6-56M12 for the natural gas compressor station "Gazli".

Further studies will aim to identify damping factors and perform fault diagnostics using an improved mathematical model of forced oscillations, realized through comprehensive use of the finite element analysis and the MATLAB/Simulink environment.

Acknowledgment

The reported results were obtained within the research project *Fulfillment of Tasks of the Perspective Plan of Development of a Scientific Direction "Technical Sciences" of Sumy State University* funded by the Ministry of Education and Science of Ukraine (state reg. no. 0121U112684) and additionally by the Ministry of Education and Science of Poland (SBAD).

References

Bachschmid, N., Pennacchi, P. and Tanzi, E. (2010). Rotor testing for crack detection, *in* N. Bachschmid *et al.* (Eds), *Cracked Rotors*, Springer, Berlin/Heidelberg, pp. 37–90.

Brunetière, N., Zahorulko, A. and Bouyer, J. (2024). Numerical simulation of the behavior of impulse gas seal, *Tribology Online* **19**(4): 360–366, DOI: 10.2474/trol.19.360.

Chelabi, M., Saga, M., Kuric, I., Basova, Y., Dobrotvorskiy, S., Ivanov, V. and Pavlenko, I. (2022). The effect of blade angle deviation on mixed inflow turbine performances, *Applied Sciences* **12**(8): 3781, DOI: 10.3390/app12083781.

Dong, L., Zhou, R., Liu, H., Zhang, L., Dai, C., Mao, Y. and Hu, J. (2022). Effect of rotational speed on unstable characteristics of lobe hydrogen circulating pump in fuel cell system, *International Journal of Hydrogen Energy* **47**(50): 21435–21449, DOI: 10.1016/j.ijhydene.2022.04.248.

Elsamanty, M., Ibrahim, A. and Salman, W. (2023). Principal component analysis approach for detecting faults in rotary machines based on vibrational and electrical fused data, *Mechanical Systems and Signal Processing* **200**: 110559, DOI: 10.1016/j.ymssp.2023.110559.

Garpelli, L., Alves, D., Cavalca, K. and de Castro, H. (2023). Physics-guided neural networks applied in rotor unbalance problems, *Structural Health Monitoring* **22**(6): 4117–4130, DOI: 10.1177/14759217231163081.

Gawde, S., Patil, S., Kumar, S., Kamat, P., Kotecha, K. and Abraham, A. (2023). Multi-fault diagnosis of industrial rotating machines using data-driven approach: A review of two decades of research, *Engineering Applications of Artificial Intelligence* **123**(A): 106139, DOI: 10.1016/j.engappai.2023.106139.

Hato, S. (2023). *Rotor Balancing: Fundamentals for Systematic Processes*, Springer Vieweg, Berlin/Heidelberg, DOI: 10.1007/9783662660492.

Hui, W., Yan, G., Shevchenko, S., Shevchenko, M., Humeniuk, T. and Buzoveria, N. (2024). General approach to the construction of non-contact seals dynamic characteristics, *Proceedings of the Romanian Academy A* **25**(4): 325–334, DOI: 10.59277/PRA-SER.A.25.4.09.

Ivanov, V., Botko, F., Dehtiarov, I., Kocisko, M., Evtuhov, A., Pavlenko, I. and Trojanowska, J. (2022). Development of flexible fixtures with incomplete locating: Connecting rods machining case study, *Machines* **10**(7): 493, DOI: 10.3390/machines10070493.

Kalkat, M., Yıldırım, Ş. and Uzmay, I. (2003). Rotor dynamics analysis of rotating machine systems using artificial neural networks, *International Journal of Rotating Machinery* **9**(4): 255–262, DOI: 10.1155/S1023621X0300023X.

Kirchgäßner, B. (2016). Finite elements in rotordynamics, *Procedia Engineering* **144**: 736–750, DOI: 10.1016/j.proeng.2016.05.079.

Kondus, V., Puzik, R., German, V., Panchenko, V. and Yakhnenko, S. (2020). Improving the efficiency of the operating process of high specific speed torque-flow pumps by upgrading the flowing part design, *Journal of Physics: Conference Series* **1741**(1): 012023, DOI: 10.1088/1742-6596/1741/1/012023.

Laine, S., Haikonen, S., Tiainen, T. and Viitala, R. (2023). Rotor resonance avoidance by continuous adjustment of support stiffness, *International Journal of Mechanical Sciences* **270**: 109092, DOI: 10.1016/j.ijmecsci.2024.109092.

Lee, D.-S. and Choi, D.-H. (1997). A dynamic analysis of a flexible rotor in ball bearings with nonlinear stiffness characteristics, *International Journal of Rotating Machinery* **3**(2): 73–80, DOI: 10.1155/S1023621X97000080.

Ma, L., Wang, J. and Li, C. (2021). Vibration suppression of a rotor system with a nonlinear MR damper, *Archive of Applied Mechanics* **91**(9): 4053–4068, DOI: 10.1007/s00419-021-01993-3.

Makivskyi, O., Kondus, V., Pitel, J., Sotnyk, M., Andrusiak, V., Polkovnychenko, V. and Musthai, M. (2024). The influence of the design features of the submersible pump rotor on the vibration reliability, *Journal of Engineering Sciences (Ukraine)* **11**(1): D1–D9, DOI: 10.21272/jes.2024.11(1).d1.

Manikandan, R. and Rajasekhara, R. (2025). Fault classification in rotor-bearing system using advanced signal processing and machine learning techniques, *Results in Engineering* **25**: 103892, DOI: 10.1016/j.rineng.2024.103892.

Nogill, P. (2019). A new single-plane balancing method based on equations of motion, *Journal of the Korean Society for Precision Engineering* **36**(6): 583–590, DOI: 10.7736/KSPE.2019.36.6.583.

Pavlenko, I., Neamtu, C., Verbovyi, A., Pitel, J., Ivanov, V. and Pop, G. (2019). Using computer modeling and artificial neural networks for ensuring the vibration reliability of rotors, *2nd International Workshop on Computer Modeling and Intelligent Systems (CMIS 2019), Aachen, Germany,* pp. 702–716.

Pavlenko, I. and Symonovskyi, V. (2015). *Critical Frequencies of the Rotor*, Computer program, Certificate of Authorship No. 59855, Ukraine.

Ran, L., Halim, D., Thein, C. and Galea, M. (2024). Lateral vibration attenuation of a rotor system using an axial control mechanism with resonance detuning, *Mechanical Systems and Signal Processing* **211**: 111220, DOI: 10.1016/j.ymssp.2024.111220.

Rao, J. (2011). Finite element methods for rotor dynamics, *in* J. Rao (Ed.), *History of Rotating Machinery Dynamics*, Springer, Dordrecht, pp. 269–297.

Roshchupkin, O. and Pavlenko, I. (2025). *EVROC: Evaluation of Rotor's Critical Frequencies—Calculation of Rotor Critical Frequencies*, Computer program, Certificate of Authorship No. 7541, Ukraine.

Stelmakh, A., Kostyunik, R., Mikosianchyk, O., Kushchev, A., Ibraimov, T., Sydorenko, O., Zaichuk, N. and Shymchuk, S. (2023). Improvement of operational parameters for precision rolling bearings by cleaning working surfaces from micro pollution of various nature, *Journal of Engineering Sciences* **10**(1): A31–A40, DOI: 10.21272/jes.2023.10(1).a5.

Suryawanshi, G.L., Patil, S.K. and Desavale, R.G.(2025). Fault diagnosis in rotor-bearing systems using ANN-based vibration analysis for Industry 4.0 machinery condition monitoring, *in* A. Kumar *et al.* (Eds) *Advances in Design and Automation, ICFAMMT 2024*, Springer, Singapore, pp. 289–303, DOI: 10.1007/978-981-97-5621-6_22.

Tarelnyk, V. and Martsynkovskyy, V. (2014). Upgrading of pump and compressor rotor shafts using combined technology of electroerosive alloying, *Applied Mechanics and Materials* **630**: 397–412, DOI: 10.4028/www.scientific.net/AMM.630.397.

Yu, Z., Shevchenko, S., Radchenko, M., Shevchenko, O. and Radchenko, A. (2022). Methodology of designing sealing systems for highly loaded rotary machines, *Sustainability* **14**(23): 15828, DOI: 10.3390/su142315828.

Zahorulko, A., Pozovnyi, O. and Peczkis, G. (2023). Experimental and CFD analysis of static and dynamic rotor stabilities in three-annular seals, *Tribology International* **185**: 108566, DOI: 10.1016/j.triboint.2023.108566.

Zhang, S., Xing, Y., Xu, H., Pei, S. and Zhang, L. (2020). An experimental study on vibration suppression of adjustable elliptical journal bearing-rotor system in various vibration states, *Mechanical Systems and Signal Processing* **141**: 106477, DOI: 10.1016/j.ymssp.2019.106477.



Ivan V. Pavlenko was born in 1983 in Sumy, Ukraine. He obtained his PhD in 2014 at Sumy State University in the field of dynamics and strength of machines, and his DSc in 2020 in the field of processes and equipment of chemical technology. Since 2009 he has been with that university, with the Department of Computational Mechanics named after Volodymyr Martsynkovskyy as an assistant professor (2009–2014), a senior lecturer (2015–2016), an associate professor (2017–2020), and a full professor (2021–present), as well as the vice dean for scientific work of the Faculty of Technical Systems and Energy-Efficient Technologies (since 2018). In 2014, he was awarded the accredited title of International Engineering Educator, Ing Paed IGIP (International Society for Engineering Education). His scientific interests concern the development of hybrid methods for parametric identification of hydromechanical systems using artificial intelligence systems. He has (co)authored over 450 scientific and methodological works, including over 150 publications in Scopus (Hirsch index of 29), four monographs, 35 patents and certificates of authorship, and six textbooks. He is a laureate of the Prize of the Verkhovna Rada of Ukraine for his scientific work on a new paradigm for the development of intelligent systems for parametric identification of technological processes.



Oleksandr V. Roshchupkin was born in 1984 in Sumy, Ukraine. He obtained his MSc degree in manufacturing engineering, machines and tools in 2006, his MSc in computer science in 2011, and MSc in computational mechanics in 2023 at Sumy State University. His scientific interests concern the integration of modern computational approaches with engineering sciences and developing models and methods for intelligent evaluation of dynamic characteristics for centrifugal machines' rotors. Since 2024, he has been a PhD student of industrial machinery engineering at the Department of Computational Mechanics named after Volodymyr Martsynkovskyy of Sumy State University.

Marek Ochowiak received his MSc in 1998 in chemical technology from the Poznań University of Technology (PUT), specializing in chemical power sources. He earned his PhD in 2002 from the Faculty of Chemical Technology at the PUT in the field of chemical technology, and his DSc degree in 2014 in chemical engineering at the Silesian University of Technology. In 2024, he was awarded the title of a full professor of engineering and technical sciences by the President of the Republic of Poland. He is currently employed at the Institute of Technology and Chemical Engineering, in the Department of Chemical Engineering and Apparatus of the PUT. He also serves as the head of the department. His scientific interests include liquid atomization in one- and two-phase systems, nozzle and nebulizer design, modeling of chemical apparatus, mass transfer processes, and the application of artificial neural networks for modeling sedimentation and dewatering processes. His recent work focuses on optimizing spray systems and enhancing the efficiency of in-

dustrial separation and fluid flow systems. He has (co)authored over 120 scientific publications, including several papers indexed in Scopus and the Web of Science, as well as in high-impact journals. His research work has been cited over 1,100 times, with an h-index of 19. He is also a co-author of several monographs, books, and patent applications. He has served as the chairman of the organizing committee for the international conference on *Practical Aspects of Chemical Engineering (PAIC)*. He is also an active member of the Chemical and Process Engineering Committee of the Polish Academy of Sciences.

Andżelika Krupińska was born in 1991 in Grodzisk Wielkopolski, Poland. She obtained her PhD in 2020 at the Poznań University of Technology (PUT) in the field of chemical sciences. Since 2019 she has been with the Department of Chemical Engineering and Equipment at the Faculty of Chemical Technology of the PUT as an assistant lecturer (2020–2022) and assistant professor (2022–present). Her scientific interests concern the spraying process, multiphase flows, chemical equipment, materials science and mechanical engineering. She has (co)authored over 220 scientific and methodological works, including 56 publications in Scopus (Hirsch index of 9) and 165 chapters in scientific monographs.

Michał Doligalski was born in 1982 in Poland. He earned his PhD in 2011 from the Faculty of Computer Science, Electrical Engineering, and Automation of the University of Zielona Góra, specializing in embedded systems. He is currently employed as an assistant professor at the Institute of Metrology, Electronics, and Computer Science of that university. His scientific interests include embedded systems, the Internet of things (IoT), satellite navigation systems, and multidisciplinary research in computer science and biomedical engineering. He is the author of numerous publications and a co-author of patents related to biomedical engineering and GNSS systems. His projects and academic related interests are to applied research in collaboration with the industry. Currently, he focuses on systemic solutions in legislation and the design and implementation of digitalization solutions for higher education and scientific institutions.

Jacek Tkacz was born in 1974 in Poland. He received his PhD degree from the University of Zielona Góra in 2008. He is currently the head of the Department of Computer Engineering and the Internet of Things at the Institute of Metrology, Electronics and Computer Science of that university. His research interests include symbolic methods of theorem proving and their practical applications in computer science and electronics. He is also interested in modern technologies for software design and development, with particular emphasis on embedded systems and mobile applications. From 1997 to 2005, he participated in the design and development of software systems for Polish libraries (PROLIB). His current research and professional activities focus on the design and development of dedicated software solutions for industrial applications. He is also the founder and owner of a software development company (IT-DSS).

Received: 15 July 2025
Revised: 2 March 2026
Accepted: 18 March 2026